Study of hydrogen diffusivity in equiatomic TiVZrNbHf high entropy alloy for hydrogen storage applications

by

K. Jarc

to obtain the degree of Master of Science
at the Delft University of Technology,
to be defended publicly on November 11th, 2022 at 1:30 PM.

Student number:	4747534
MSc track:	Materials for sustainable development
Supervisor:	Dr. A. J. Böttger
	Dr. M. H. F. Sluiter
Thesis committee:	Dr. P. Dey TU Delft committee, 3ME

TU Delft

Abstract

High entropy alloys (HEAs) are new potential materials for hydrogen storage applications which could help with the transition towards sustainable energy sources. The rate of hydrogen kinetics is one of the material properties that is important for the storage and other hydrogen related applications. One of the limiting factors on the rate of hydrogen kinetics is hydrogen diffusivity. Thus far, there has been no reports on hydrogen diffusivity for HEAs in relation to hydrogenation kinetics. Therefore, this project investigates hydrogen diffusivity in equimolar TiVZrHfNb and the influence of hydrogen concentration on hydrogen diffusivity to gain better understanding of hydrogenation kinetics. The selected HEA has been found to absorb the highest amount of hydrogen (2.5 H/M) among other HEAs.

The investigation was done by a computational approach using ab initio molecular dynamics. BCC and face-centered cubic (FCC) supercells with different hydrogen concentrations (H/M = 0.2, 0.8, 1.4, 2, 2.4) were simulated at a temperature range of 773 – 973 K. At the same time, experimental electrochemical hydrogen charging using chronoamperometry and cyclic voltammetry was performed in order to compare computational and experimental values of hydrogen diffusivity.

The electrochemical hydrogen charging did not result in hydrogen absorption, most probably due to the passivation of the sample surface.

From the simulation results, the values of activation energy and pre-exponential factor were estimated to be in the range of 0.26 – 0.48 eV and 0.73 – 2.95 $\times 10^{-7}\, m^2/s$, respectively. Hydrogen diffusivity was found to be higher in BCC than in FCC. In BCC the hydrogen diffusivity slowly decreases linearly with increasing H/M. In the case of FCC, the hydrogen diffusivity was found to be the highest at 2.4 H/M while at 2 H/M the diffusivity was the lowest. The analysis of hydrogen occupation at 2 H/M shows that most of the hydrogen atoms are trapped inside tetrahedral sites. It is possible that the hydrogen occupation in the tetrahedral sites results in the optimum hydrogen distribution where the repulsive interaction between hydrogen atoms is the lowest. At concentrations above 2 H/M, an additional repulsive force between hydrogen atoms seems to contribute to the increase of hydrogen diffusivity.

Contents

List of Figures vii

List of Tables ix

1 Introduction 1
1.1 Background . . . 1
1.1.1 High entropy alloys: New concept of alloy design . . . 3
1.2 State-Of-Art research on hydrogenation properties of HEA . . . 5
1.2.1 Factors influencing the H storage properties . . . 5
1.2.2 Hydrogen storage properties of TiVNbZrHf . . . 8
1.3 Problem statement . . . 9
1.4 Research objective and approach . . . 9

2 Methodology 11
2.1 Sample preparation and characterization . . . 11
2.2 Electrochemical hydrogen charging procedure . . . 13
2.3 Computational methods . . . 16

3 Results and Discussion 19
3.1 As-cast sample analysis . . . 19
3.2 Electrochemical hydrogen charging results . . . 23
3.2.1 Pre-charging conditions . . . 24
3.2.2 Charging results . . . 24
3.3 Molecular dynamics simulation results . . . 30
3.3.1 TiVZrNbHf without hydrogen . . . 30
3.3.2 Stability of molecular dynamics runs . . . 31
3.3.3 Hydrogen diffusivity and activation energy . . . 31
3.3.4 Hydrogen preferential site occupation . . . 36

4 Conclusions 39

5 Recommendations 41

Bibliography 43

List of Figures

1.1 General overview of thus far known hydrogen storage systems and their typical storage properties; the major trends of research are represented with green [33]. 2
1.2 Visual comparison of amount of hydrogen energy stored per volume (energy released when H_2 reacts with O_2 [kWh/L]) and volumetric density [g H_2/L] for a) physical and b) chemical hydrogen storage systems Hassan et al. [25]. 2
1.3 Typical crystal structures of interstitial hydrides where hydrogen (red dots) can occupy octahedral (O-sites) or tetrahedral sites (T-sites); materials with BCC structure can in theory have 3 H/M (number of hydrogen atoms per metal atom) for octahedral (O-sites) and 6 H/M for tetrahedral sites (T-sites) while FCC can only have 1 H/M for O-sites and 2 H/M for T-sites [41]. . . . 3
1.4 The fraction of occupied tetrahedral sites in relation to the valence electron concentration (VEC), of the four nearest neighbor metals in the RMC structure model of a) $TiVNbD_{5.7}$ [48] and b) $TiVCrNbD_{2.2}$ [49]. Arrows are added in the plots to highlight the decreasing trend of site occupancy with increasing VEC. 7

2.1 Arc melting unit for the sample synthesis. 12
2.2 As-cast sample - a) droplet shape; b) blue dashed line - vertical and c) orange dashed line - horizontal cross sections. 13
2.3 Final look of prepared sample for electrochemical H charging experiments. 14
2.4 Final look of prepared sample for electrochemical H charging experiments. 14

3.1 SEM images of the analyzed samples recorded with BSE. The squares mark the areas measured by EDS. 19
3.2 SEM-BSE images of as-cast sample a) horizontal (x 60) and b) vertical cross section (x 30). 20
3.3 Images of elemental distribution obtained with EDS mapping. The measurements of two different areas in the sample S8 where some variation in the distribution is observed. 20
3.4 Line EDS analysis of (1) interdendritic and (2) dendritic region of as-cast sample as indication of some variation in chemical composition. 21
3.5 XRD patterns for sample S6 (top), S8 (middle) and S9 (bottom). The red sticks give the peak positions and intensities of the possibly present crystalline phases, using the ICDD pdf4 database; intensity scale is square root. 22
3.6 Pourbaix diagram for Ti (obtained from materialsproject.org [55]). The blue arrow indicate the charging potential (V vs. SHE) for the selected pH where hydrogenation of Ti starts; the top orange dashed line marks oxygen evolution reaction (OER) and the bottom line marks hydrogen evolution reaction (HER). 23
3.7 Comparison between cyclic voltammograms of (a) Ti [46] and (b) the TiVZrNbHf sample from -1.7 V to 0.6 V vs. $Ag/AgCl_{sat}$ at 100 mV/s; the 1st scan shows irreversible oxidation peak. 24
3.8 Charging results: (a) charging curve at -1.7 V vs $Ag/AgCl_{sat}$ for 1h and (b) CV scans at 20 mV/s before and after charging. 25
3.9 Voltammograms obtained after charging for 1 h at different potentials. The arrow indicates decreasing values of anodic part of the curve as set charging potentials are higher. 25
3.10 CA results (from the first 72 h of charging) from three separate H charging for extended period of time with the applied potential of -1.55 V; A-72, B-168 and C-450 denote charging runs for 72 h, 168 h and 450 h respectively. 26
3.11 XRD patterns of the sample before and after H charging for 72 h; intensity scale is square root. . 27
3.12 XRD patterns of the sample before (blue) and after H charging for 19 days (black) including results from wobbling (red); the middle XRD pattern shows close-up of the (200) split peak. The bottom figure shows XRD pattern for the charged sample after surface cleaning. 29
3.13 Simulation cell of the relaxed BCC (left) and FCC (right). 30

3.14 Average values of total energy (E_{tot}) in each quarter of analyzed run time - BCC (top) and FCC (bottom). 31
3.15 Mean square displacement (MSD) for metal atoms in TiZrHfVNb as a function of time; obtained from BCC (left) and FCC (right) MD simulation with 175 H at 973 K. 32
3.16 Mean square displacement (MSD) with linear regression fit for H atoms in TiZrHfVNb as a function of time; obtained from BCC (left) and FCC (right) MD simulation with different H concentrations at 973 K. 32
3.17 Arrhenius plot for BCC (left) and FCC (right) obtained from different H concentrations; for BCC with 25 H the diffusivity values show the most deviation from the fitted line, indicating a non-linear trend. 33
3.18 Values for D_0 (left) and E_a (right) are plotted as a function of H/M; the error bars show 95 % confidence interval. 33
3.19 Diffusivity values as a function of H/M for BCC and FCC at different temperature. 35
3.20 Diffusivity values for H in FCC plotted against H/M. 35
3.21 Histograms for H occupation times inside T- and O-sites before a jump for FCC at 873 K; for 1.4 and 2.4 H/M have an additional enlarged area to show counts for longer times. 36
3.22 Occupation times for each individual H atom; the first column dt(avr) shows average time that a H atom occupies a site and the second column shows average time of a H atom occupying T- and O-sites; last column dt(max) is maximum time found for a H atom to occupy T- and O-site. The times were obtained for FCC at 873 K. 37

List of Tables

2.1 Material specifications, melting T of elements and calculated weights. 11
2.2 Parameters of arc-melting sample preparation. 12
2.3 CV and CA settings used in each run of the first approach for H charging; potential values are expressed against $Ag/AgCl_{sat}$. 15
2.4 Overview of the MD runs for BCC and FCC; H_x is the total number of hydrogen atoms in the supercell, t is a total simulation run time and τ is a time interval taken from the end part of the total simulation run time (used for analysis). 17
2.5 Overview of the additional MD runs for FCC; H_x is the total number of hydrogen atoms in the supercell, t is a total simulation run time and τ is a time interval taken from the end part of the total simulation run time (used for analysis). 18

3.1 Chemical composition (at.%) of the selected as-cast samples analyzed by EDS mapping (regions indicated in 3.1) and XRF. 21
3.2 Chemical composition (at%) of average, dendritic and interdendritic region analyzed by line EDS, indicated in 3.4. 21
3.3 Normalization factor (f_{norm}) for the 1st nearest neighboring (1 st NN) pairs for the BCC and FCC simulation cell. 30
3.4 Diffusivity (D_H), pre-exponential factor (D_0) and activation energy (E_a) for H in TiVZrNbHf obtained from the slope of MSD using Einstein relation; the data used for calculation of the values was taken from the last time interval τ (Table 2.4). 34

1 Introduction

1.1. Background

Increasing demand for energy while minimizing environmental impact make switching from non-renewable to renewable energy more than ever a necessity. As an energy carrier hydrogen seems an attractive alternative to fossil fuels. However, wide application of hydrogen requires development of new infrastructure and technology. The critical part of such energy transition is development of reliable, transportable, and cost efficient hydrogen storage technology.

A part of research efforts is a development of hydrogen storage materials and systems that meets the following criteria set by US Department of Energy (DOE) for a light-duty vehicle [1, 32]:

- High gravimetric (> 5 wt.%) and volumetric H-capacity (> 40 g H_2/L)
- Easy activation
- Fast kinetics (flow rate of 0.02 g H_2/s for one kW)
- Discharging at moderate pressures (5-12 bar) and temperature (-40/85 °C) which requires reaction enthalpy to be between 27 and 41 kJ/mol
- Good stability against contaminants and environmental factors (moisture, temperature changes, etc) to be able operate at 85 % from initial capacity over a lifetime
- Good reversible cycle performance (storage does not lose its initial properties below DOE set targets for over 1500 cycles)
- Inexpensive production (the final cost of H_2 and a storage material should be competitive with other commercially available fuel systems, e.g. hybrid vehicles)

Over the years, different storage systems have been developed with the aim of fulfilling those requirements. A general classification of those systems is presented in Figure 1.1

The current research trends of the storage technologies are mostly focused on on-board reversible material-based storages. The major advantage over physical storage is that solid-state hydrogen absorbers are safer and have the ability to store high amount of hydrogen in a small volume (Figure 1.2). The reason for such high volumetric density is due to bonding of atomic hydrogen with the material.

One of the most researched hydrogen absorption materials with the potential to meet the hydrogen storage requirements are interstitial metal hydrides. Compared to other reversible chemical materials for on-board applications, metal hydrides are known for having high volumetric storage capacity (defined as maximum amount of H released from the total volume of material [g H_2/L], as presented in Figure 1.2).

Some transition metals have been long known for their ability to store high amount of hydrogen due to a metallic structure where H atoms can occupy interstitial positions. Especially the metals with BCC-type structure where metal atoms are not as closely packed as in HCP or FCC structure (Figure 1.3 shows possible H occupation within the three most common crystal structures for metals). However, the transition metals

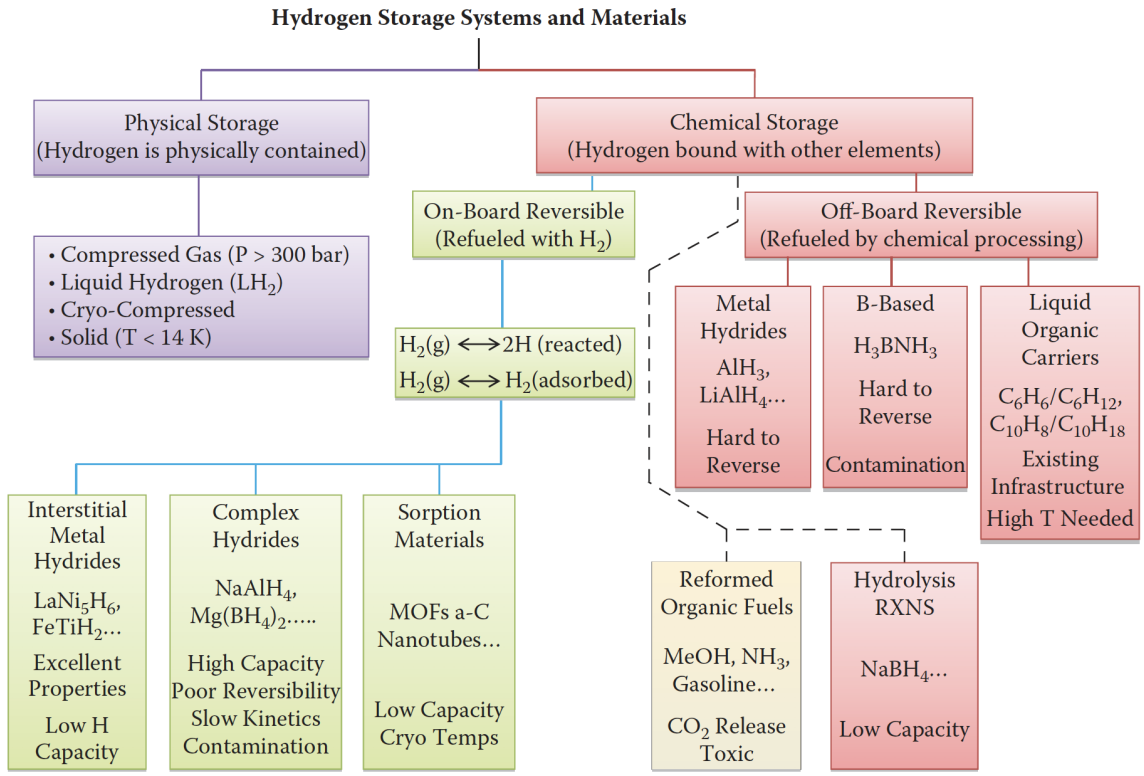

Figure 1.1: General overview of thus far known hydrogen storage systems and their typical storage properties; the major trends of research are represented with green [33].

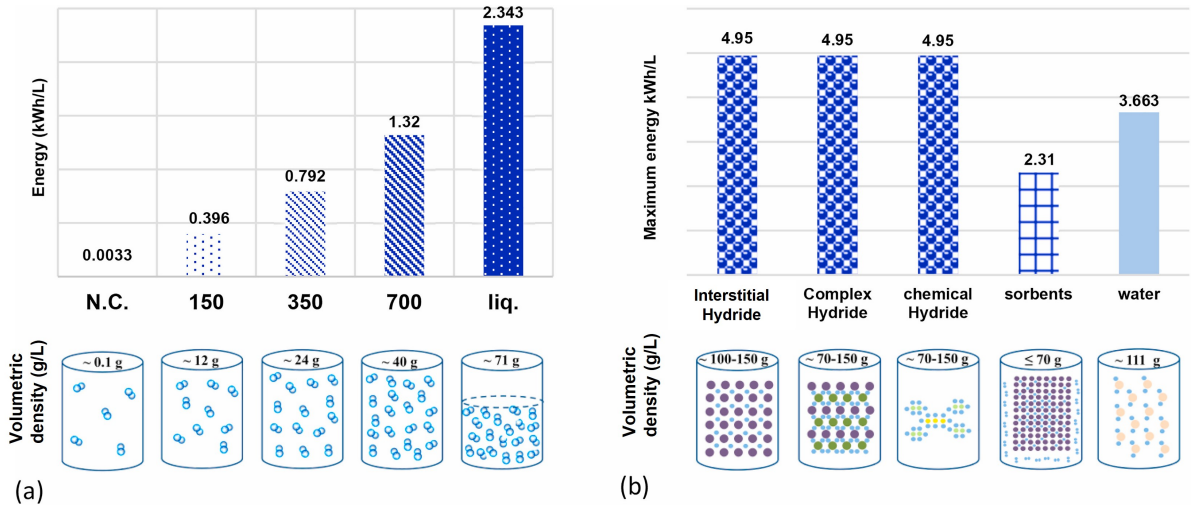

Figure 1.2: Visual comparison of amount of hydrogen energy stored per volume (energy released when H_2 reacts with O_2 [kWh/L]) and volumetric density [g H_2/L] for a) physical and b) chemical hydrogen storage systems Hassan et al. [25].

are very heavy which results in low gravimetric hydrogen density (weight percentage of absorbed H compared to the total weight of the storage material and amount of H absorbed).

Apart from the low gravimetric hydrogen density, transition metals in a pure form have poor hydrogen absorption kinetics, poor reversibility due to high stability of hydrides. Those properties can be improved by forming an alloy consisting of transition elements that form strong bonds with H (type A) and of non-hydride forming elements (type B). Several combinations of alloys containing the type A and B metals (AB, AB_2, AB_5 and BCC random solid solution) have been investigated. The metal hydrides are a promising material for H storage applications since they can store H at high density (~100-150 g/L). However, the research is still

ongoing to further reduce the material weight (increase in gravimetric hydrogen density) and to improve H absorption kinetics without affecting the volumetric H capacity [58, 59, 61, 63].

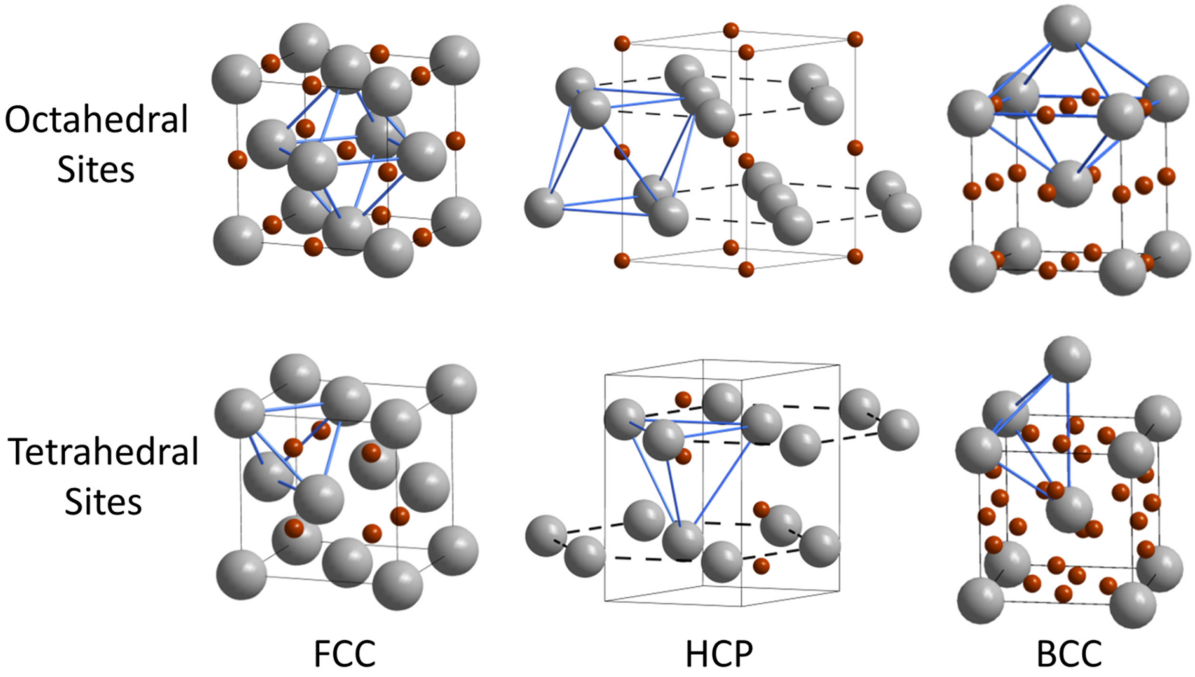

Figure 1.3: Typical crystal structures of interstitial hydrides where hydrogen (red dots) can occupy octahedral (O-sites) or tetrahedral sites (T-sites); materials with BCC structure can in theory have 3 H/M (number of hydrogen atoms per metal atom) for octahedral (O-sites) and 6 H/M for tetrahedral sites (T-sites) while FCC can only have 1 H/M for O-sites and 2 H/M for T-sites [41].

1.1.1. High entropy alloys: New concept of alloy design

High entropy alloys (HEAs) are a new class of material, originally defined by Yeh et al. [74] as alloys consisting of five or more elements of approximately equiatomic concentrations[1]. This definition is based on a hypothesis that the formation of single-phase solid solution can be stabilized due to high mixing entropy.

For simple binary systems a degree of solubility can be used to predict whether an alloy will form substitutional, interstitial solid solution or intermetallic compound. The Hume-Rothery rules suggest that atomic radii, crystal structure, valency and electronegativity are the factors governing the solubility between metal elements; when a solute metal has similar atom radii (less than 15 % difference), crystal structure, valency and electronegativity as a solvent metal, the complete solubility is expected which leads to formation of single-phase substitutional solid solution. However, the rules cannot be extended to multicomponent systems. It was generally accepted that multicomponent alloys can only form multiple phases with undesirable brittle intermetallics which was the reason for the multicomponent alloys to be scarcely researched.

Yeh et al. [74] and Cantor et al. [8] first reported on HEAs forming single-phase solid solution with significant improvement of mechanical properties. Since then, these unexpected results have encouraged the material research to investigate previously unexplored area of HEAs. The research highlights over the last two decades can be found in these comprehensive overviews on HEAs [6, 23, 24, 27, 37, 39, 52, 69, 75].

The formation of a single-phase solid solution with simple crystal structures and surprising properties observed in HEAs, seems to be influenced by several chemical and physical factors as a result of multi-elemental environment. Jien-Wei [28] proposed configurational entropy, sluggish diffusion, cocktail effect and lattice distortion to have the main effects on the properties of HEAs as will be explained next:

High entropy effect describes the effect of configurational entropy on stability of single-phase formation in random solid solutions. The configurational entropy (ΔS_{conf}) is a term describing a number of ways (w)

[1]There is no universal agreement on HEA definition; some of the reasons are presented in the critical review by Steurer [69]

particles can be arranged in a crystal structure and is calculated by Boltzmann's equation

$$\Delta S_{conf} = k_B \ln\ w = -R \sum_{i=1}^{n} X_i \ln X_i \tag{1.1}$$

where k_B is Boltzmann's constant. ΔS_{conf} can be also expressed in terms of contributions from each mole fraction X_i of ith out of n components in random solid solution, where R is the gas constant; when the mole fraction of each component is the same the equation for ΔS_{conf} in equimolar alloys is calculated as

$$\Delta S_{conf} = R \ln n \tag{1.2}$$

The Gibbs free energy of mixing ΔG_{mix} determines the change of the system energy as a result from mixing two or more elements (when ΔG_{mix} is negative, there is a preference to form bonds between unlike atoms) and depends on the mixing enthalpy ΔH_{mix} and the mixing entropy[2] ΔS_{mix} at temperature T through the following equation:

$$\Delta G_{mix} = \Delta H_{mix} - T\Delta S_{mix} \tag{1.3}$$

The term ΔH_{mix} represents the energy change between energy required to break bonds of alike atoms to form bonds with unlike atoms. Based on the regular solution model [80], the general equation for ΔH_{mix} with n elements in the mixture is

$$\Delta H_{mix} = \sum_{i=1, i\neq j}^{n} \Omega_{ij}\, x_i x_j \tag{1.4}$$

where Ω_{ij} (= $N_A\, z\, \Delta H_{mix}^{ij}$)[3] is the regular solution parameter of ith and jth element based on the total mixing enthalpy of $i-j$ alloy ΔH_{mix}^{ij} (=$H_{ij} - \frac{1}{2}(H_i + H_j)$) and $x_i x_j$ are the atomic percentages of the ith and jth component (represent the probability of ith and jth component to form a bond). From Equation 1.2 Equation 1.2 shows that ΔS_{mix} increases with the number of elements in the mixture while ΔH_{mix} becomes less negative based on Equation 1.4 and the assumption that all binary compounds have the same mixing enthalpy. Therefore, the term $T\Delta S_{mix}$ in Equation 1.3 contributes more to lowering ΔG_{mix} and thus enhancing the formation of solid solution phases in HEAs.

Sluggish diffusion effect is an effect of substitutional diffusion on diffusional phase transformation kinetics in relation to the number of composing elements in HEA. Observed high temperature phases in slowly cooled HEA samples have indicated that the diffusion rate of atoms is significantly limited compared to conventional metals. Slow substitutional diffusion causes retardation of phase transformation and grain growth. For instance, elements Ti, Zr and Hf have BCC at high temperature and HCP structure at room temperature. However, most of the Ti-Zr-Hf based HEAs form solid solution with BCC structure which is believed to result from very slow diffusion of atoms [65]. It has been suggested that the observed sluggishness of HEA is due to greater fluctuation of lattice potential energy (caused by different chemical environment) leading to variation of jump barriers which hinders the atomic movement [70]. This has been contributed to improvement of several different properties, such as improved mechanical properties, better thermal stability, etc. However, as summarized in a critical review by Divinski et al. [14], the sluggish diffusion effect in HEAs as one of the core effects seems to be misleading since the observed slow kinetics rely on indirect observations (comparison of an alloy structure before and after annealing) and not on direct observations (measurement of diffusion).

Cocktail effect refers to the enhancement of properties from individual elements in the alloy composition. In conventional alloys posses the main properties of the dominating element where certain properties, can be improved by addition of minor elements as a sum of the properties of elements. Contrary, in HEAs all elements are equally represented and thus contribution from each element to the alloy properties cannot be as easily determined as in conventional alloys. As an example of HEAs unpredictable nature, equimolar TiVZrNbHf solidifies into BCC structure despite the majority of the constituent elements (Ti, Zr and Hf) in a pure form have HCP structure at room temperature. It has been suggested that HEAs exceptional properties can exceed the sum of basic properties of the constituent element due to addition of divers interactions between all the elements (e.g. combination of super elasticity and plasticity).

[2] The term ΔS_{mix} consists of configurational, vibrational, electronic, and magnetic entropies. However, apart from the configurational, the rest of the entropies have negligible contributions to the ΔS_{mix}.

[3] Avogadro's number N_A, coordination number of 1st neighboring atoms in the crystal structure z.

Most studies that investigate material for specific application (e.g improving H absorption/desorption kinetics in material with high H storage capacity for H storage application) use those four effects for the interpretation of observed properties in HEAs, even though the effects are still under debate. Pickering and Jones [56] and more recently Mehta and Sohn [38], Biswas et al. [6], published articles providing more details on the issue of the HEA core effects, showing there is still a lot of unknown about HEAs. The cocktail effect has been discussed as whether it should be a part of the HEAs core effects or it serves more as a reminded that predicting a HEA final properties is not as straightforward as for conventional alloys. Dąbrowa and Danielewski [13][12, 14] addressed the absence of concrete evidence on sluggish diffusion effect and He and Yang [26] discussed the issues on the verification of lattice distortion as direct relation to the material properties.

1.2. State-Of-Art research on hydrogenation properties of HEA

The new concept of multi-principal element alloys has become popular way of improving material properties for different applications. Since the first mention of the HEAs, majority of studies has focused on investigation of mechanical properties for structural applications. The recent advancement in research on HEAs has increased interest also on other application areas. One of the recently discovered areas are metal hydrides for hydrogen storage application, where HEAs have showed to perform better than conventional alloys.

The hydrogen storage properties of metal hydrides show strong relation to the initial crystal structure; metals with the same structure have been shown to have similar trend in hydrogen properties. The main HEA structure types that have been investigated the most for hydrogen storage applications are HCP (Laves) and BCC phase. Each structure group shows the following trends:

- **Laves (HCP) phase** HEA has fast absorption kinetics and can be easily activated at room temperature but do not show capacities higher than 1 $H/M_{(max)}$ and show poor reversibility[4] [10, 15, 21, 30, 34, 64, 76].

- **BCC phase** HEA has much higher hydrogen capacity (BCC structure have the most (theoretically) available interstitial positions per unit cell (Figure 1.3) thus can store high amount of hydrogen) but needs to be activated at high temperature and has slower kinetics than laves phase HEA; the latest studies show there is a potential to further improve those properties [36, 42–45, 51, 67, 68, 77–79].

Among these two groups, the BCC type HEAs show more potential for further improvements (such as kinetics and activation process) than HCP type HEAs. therefore, the focus of the following overview will be the research progress of HEAs with BCC structure for hydrogen storage applications.

1.2.1. Factors influencing the H storage properties

Unique hydrogen storage properties and behavior, have been observed in HEAs compared to traditional metal hydrides. Since the research field is still young, the relations between HEAs properties and H behavior are still not completely understood. The main reason for this is the complexity of the multi-elemental environment in HEAs where a number of different elemental configurations creates a variation in local properties. Thus, it is challenging to identify which factors affect certain H property. Nevertheless, the research observations and comparison with traditional metal hydrides already provides some clues towards better understanding for HEAs improved H storage properties. For instance, most of HEAs show a sloping plateau pressure in the PCT plots which has been already observed in conventional BCC random solid solutions (hereinafter referred to as BCC alloys) [62]. This has been related to the difference in interstitial affinity for H as a result of random distribution of elements in the lattice structure. The sites in such alloys are not energetically equivalent as in conventional binary hydrides and thus H occupies/leaves certain position under different charging/discharging conditions. However, compared to BCC alloys the HEAs show improvement in kinetics and thermodynamic hydrogen absorption/desorption properties as well as larger hydrogen storage capacity.

Improvements of hydrogen storage properties of HEAs compared to conventional alloys, are well portrayed in the study of Nygård et al. [51]; compared to ternary TiVNb alloy, an addition of just one element

[4] As an exception to the Laves HEAs, Floriano et al. [22] discovered that the combination of Laves and minor BCC phase in TiZrNbCrFe alloy can increase $H/M_{(max)}$ and improves reversibility.

to TiVNb-based HEA improved desorption kinetics as well as reversible hydrogen storage capacity. In another study based on simulation results, Nygård et al. [48] observed changes in H site occupation for each additional element (Zr, Hf) in TiVNb-based HEA.

It has been suggested that lattice distortion [17, 50, 60, 78, 82], global and local valence electron concentration (VEC) [17, 49, 51, 67] and sample initial state [17, 35, 42, 43, 66–68, 77, 79], affect hydrogen storage properties of HEAs:

Lattice distortion The appeal of HEAs as a promising hydrogen storage material arises from the assumption of HEAs having high lattice strain. Recent theoretical studies on metal hydrides [29, 73] show that the presence of a lattice strain alters energies between sites, which can lead to more interstitial sites become accessible for H to occupy. This has stimulated the idea of HEAs as a potential candidate for hydrogen storage applications since HEAs show to have highly distorted lattice and could therefore be beneficial to further increase H/M.

Indeed, many authors suggest that lattice distortion in HEAs is responsible for improved hydrogen storage properties compared to traditional hydrides. For instance, Zhang et al. [79] claims that lattice distortion introduces more lattice defects which improves absorption kinetics observed in $TiZrHfNb_2$; mismatch between different atom sizes increases distance between metal atoms, which lowers energy barrier thus H requires less energy to successfully jump through the barrier, leading to lower activation energy and faster absorption. Zhang et al. [77] investigated the effect of activation procedure on absorption of equimolar TiZrNbTa. The authors associated the HEA activation behavior with the lattice distortion effect for which it is expected to be responsible to cause higher amount of lattice defects, even before activation. The investigation showed that defects (most likely vacancies), formed during the absorption, were retained in the material after desorption, which is different from traditional alloys. It has been suggested that the sluggish self-diffusion of the HEA impedes the lattice from returning to the initial condition, thus the defects are retained after H desorption.

The experimental results show that HEA systems can transform into fully hydrogenated hydride directly from BCC to FCC/BCT [42, 44, 45, 60, 66], possibly due to lattice distortion effect. According to Zlotea et al. [82], for larger distortions a hydride forms in one-step phase transition while for alloys with smaller distortions, such as TiZrNbHfTa, the hydride has two-steps transition (BCC → BCT → FCC), which is similar to BCC alloys. This has been suggested based on comparison between TiZrNbHfTa and TiVZrNbHf [31, 60], where Ta substitution of V lowers the value of atomic size difference (δ). In later studies [17, 79], the degree of the lattice distortion showed no correlation to step reaction of hydride for Ti-V-Zr-Nb-Hf based HEA systems.

BCC type HEAs have shown to have in general maximum H storage capacity up to 2 H/M. However, Sahlberg et al. [60] found for TiVZrNbHf to exceed these values. With 2.5 H/M ratio, the HEA shows abilities to store larger amount of H which was only observed for the light rare-earth metals. This has been indicated to be possible because the alloy is able to store H in both T- and O-sites [31, 48] due to the lattice strain. Nygård et al. [50] investigated the influence of lattice distortion on improved hydrogen storage capacity. They prepared several different Ti-V-Zr-Nb-Ta HEAs with ranging δ as a measure of lattice distortion. They could not find the correlation between lattice distortion and ability of some HEAs to store high amount of hydrogen. Even more extensive research on 21 ternary, quaternary and quinary Ti-V-Zr-Nb-Hf based alloys could not observe any relation between H capacity and lattice disorder.

Lattice distortion is mostly calculated as relative atomic size difference (δ) where atoms are assumed to be hard spheres. Nygård et al. [51] [49] assessed the extend of local lattice strain in TiVNb based HEAs through theoretical simulation. The results indicate that calculation of δ gives misleading values of the distortion magnitude since δ does not account for whether the element causing the change of δ is smaller or larger than the rest of the elements.

Valence electron concentration (VEC) Another factor that seems to play a role in hydride properties is VEC. For instance, both Nygård et al. [51] and Ek et al. [17] observed a linear increase of the volume expansion during hydride phase transformation as well as a decrease in stability of the hydride, with the increasing VEC value. Nygård et al. [51] observed that all HEAs[5] under the same charging conditions, transformed into FCC single-phase hydride when VEC < 4.75 while the alloys with VEC≥4.75 contains BCT and FCC hydride phase. The alloys with BCT hydride phase (higher VEC) also showed lower H storage capacity which indicates that such alloys require much higher pressure for the complete transformation to FCC hydride phase. For the most stable hydrides (with FCC phase), two desorption peaks have been observed upon desorption, indicating that

[5] Only TiZrNbHf is exception, forming BCT phase.

the phase transformation occurs with an intermediate BCC monohydride. Desorption results from Ek et al. [17] also showed two peaks but could not relate this to the final hydride structure and H/M ratio with VEC.

Silva et al. [67] followed up on investigation of VEC effect on H properties by preparing 3 different HEAs with the same VEC. The studied alloys showed similar values of storage capacity, enthalpy and entropy formation energy, and all have similar absorption kinetics. However, different desorption behavior between the alloys indicates that other factors seem to affect the desorption properties of HEA hydride.

For the case of $Ti_{30}V_{25}Zr_{10}Nb_{25}Ta_{10}$, Montero et al. [43] could not explain the change of onset desorption T in correlation with VEC, as Nygård et al. [51] suggested. Absorption results showed that the BCT/FCC hydride formed in a single step reaction while during desorption experiment two peaks occurred. Further investigation revealed that hydride transformed with the single step reaction, meaning that the two desorption peaks occurred as a result of intrinsic kinetics of hydride phase and not due to two phase transitions.

Theoretical investigations on deuterium preferential occupancy in TiVNb based HEAs, showed that a number of occupied sites is significantly higher for interstitials with lower local VEC than for the ones with higher VEC (Figure 1.4) [49, 51]. This could explain more than one desorption peak observed experimentally for HEAs with higher VEC. Ek et al. [17] suggested that during a desorption event, H atoms in interstitials with higher local VEC leave first, corresponding to the first desorption peak at lower temperature. Afterwards, it is possible that some deuterium atoms in T-site with higher VEC are still present but due to lower deuterium concentration, they can make a jump to lower VEC O-sites which desorb later.

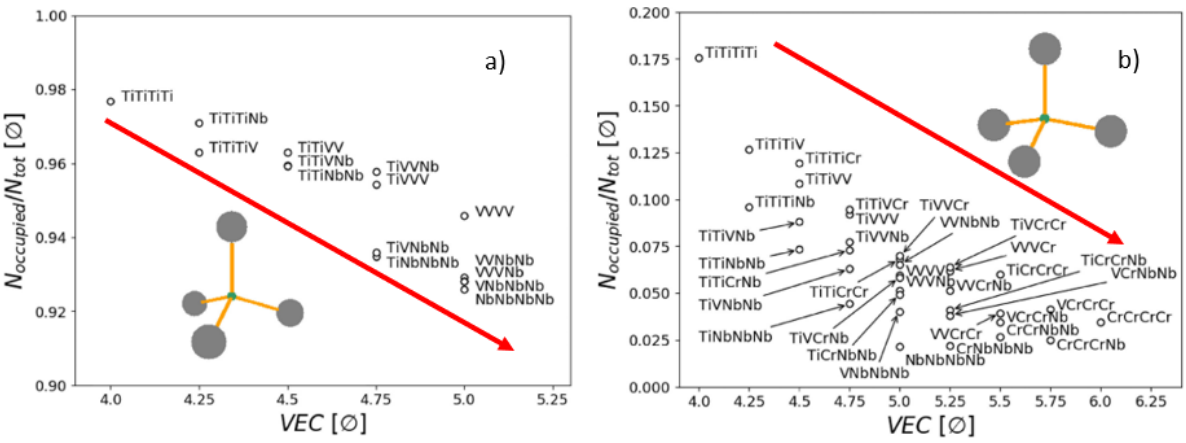

Figure 1.4: The fraction of occupied tetrahedral sites in relation to the valence electron concentration (VEC), of the four nearest neighbor metals in the RMC structure model of a) $TiVNbD_{5.7}$ [48] and b) $TiVCrNbD_{2.2}$ [49]. Arrows are added in the plots to highlight the decreasing trend of site occupancy with increasing VEC.

Initial state of a HEA Several intrinsic factors, such as disproportionation (formation of stable monohydride phases), chemical segregation, degree of crystallinity and surface passivation, can cause a decline in HEA hydrogen storage capacity. Decrease of H capacity on cyclic absorption/desorption has been observed in most studies. Some of the possible reasons for that could be segregation and oxidation during hydrogen absorption/desorption cycling, especially at T > ~500 °C [35, 45, 50, 51]. Montero et al. [43] found no indication of phase segregation in $Ti_{30}V_{25}Zr_{10}Nb_{25}Ta_{10}$ after 20 cycles. They observed slight increase of BCC and hydride lattice parameter and increase in the amount of smaller grains at the end of cycling experiment. The investigation of crystallinity size on the reduction of reversible H capacity and the results of Zhang et al. [77] study, suggests the importance of hydride preparation method on the cycling performance of HEAs as well as on H capacity.

Preparation techniques can have major influence on these factors. Few studies investigated the effect of different synthesis methods on H storage properties [35, 42, 43]. Kunce et al. [34] prepared HEAs with Laser Engineered Net Shaping (LENS). Most of the samples were not completely homogenized and the results showed strange correlation between state of samples and maximum H concentration ($H/M_{(max)}$ - absolute amount of H absorbed) for both, Laves [34] and BCC single phase [35]. As-cast samples showed higher $H/M_{(max)}$ than annealed ones. Similar results were obtained for BCC TiZrNbMoV alloy where the sample that show no dendritic segregation showed much lower hydrogen capacity. The reason for that is unclear since in later studies samples with the most segregation usually show poorer H storage performance.

Comparison of H properties between HEA prepared with mechanochemical and arc melting methods shows that all samples formed hydride in one step reaction upon absorption but samples prepared mechanochemical showed lower H/M$_{(max)}$ [42, 43]. This has been related to reduction of crystallinity and high concentration of deformations and defects introduced during ball-milling. Direct preparation of hydride through reactive ball milling under high H pressure showed better desorption properties than arc melting or ball milling. Interestingly, ball milled sample showed worse desorption behavior than arc melted sample.

An oxide layer on the alloy surface is known to act as an additional energy barrier, reducing the absorption kinetics. Zhang et al. [77] found that surface of TiZrNbTa has high valence state oxides (Ti/Zr +4, Nb/Ta +5) before activation after which the surface transformed into lower valence state sub-hydroxides (Zr +1, Ti/Nb/Ta +2). The formation of sub-hydroxides at the surface has shown to have positive effect on H diffusivity into the bulk. The alloy was able to quickly absorb H at RT; before activation sample needed T above 400 °C to start absorbing H. The same activation procedure on pure elements of the HEA, resulted in the reduction of surface oxides into sub-oxides and absorption T for all pure elements decreased but it was still above 340 °C. Based on these results and the comparison with the pure elements, it is evident that the formation of the sub-hydroxides layer greatly improves absorption conditions. The ability of the HEA to form the sub-hydroxide layer, was ascribed to increased reduction activity due to interaction variations between different elements (cocktail effect). Here it is interesting to point out that in the Nygård et al. [51] study, the activation procedure was not necessary for the TiVCrNb to absorb H, even after air exposure for days.

1.2.2. Hydrogen storage properties of TiVNbZrHf

Equimolar TiVZrHfNb has been found to posses exceptional high hydrogen storage capacity of 2.5 H/M [60]. This is unusual for metal hydrides based on transition elements, which can reach H/M ≤ 2 and only hydrides containing rare-earth elements show ability to absorb more than 2 H/M. The H/M of 2 for transition-based hydrides is (theoretically) possible if all tetrahedral interstitial sites (T-sites) are occupied. The alloy ability to absorb such high amount of hydrogen is therefore enabling occupation of octahedral sites (O-sites) as well.

Hydride formation path of TiVZrHfNb has been proposed to have a combination of the BCC and RE hydride transformation route with BCC → distorted FCC/BCT for obtaining such high H capacity. Hydride phase has been reported both as BCT and FCC structure [17]. Karlsson et al. [31] tried to identify the position of hydrogen atoms with in- and ex-situ neutron powder diffraction to confirm the hypothesis of H occupying both T- and O-sites in TiVZrHfNb, thus explaining the high H/M. In-situ experiments show no significant preference between interstitials while ex-situ experiments show that the majority of T-sites is occupied. However, the author admits that quality of these results is not very good because the neutron absorption cross section for this alloy is high and the environment of the sample caused signal interference.

Simulation result from Nygård et al. [48], provided some insight on preferential occupation of deuterium in TiVZrHfNb. The reversed Monte Carlo (RMC) models showed that D atoms prefer to occupy bigger T-sites (94 % of the total T-sites) and avoid the smaller ones. For those, the D is displaced into some O-sites (12 % of O-sites are occupied). It is interesting that D prefers T-sites that have smaller volume than O-sites in the hydride structure. The observation of δ, VEC, interstitial volume, etc. could not provide an explanation for the D simultaneous occupation of O- and T-sites in TiVZrNbHf. The distance between T- and O-sites for TiVZrHfNb, compared to TiVNb (d = 1.92 Å) and TiVZrNb (d = 1.96 Å), was found to be slightly larger (d = 1.98 Å). The Switendick criterion [72] states that the minimum H-H distance is about 2.1 Å based on the assumption that H is positioned at the center of a site. Since the lattice distortion is present in TiVZrHfNb and the distance between T- and O-sites for TiVZrHfNb is based on the average lattice parameter, some of the T-O distances might be large enough to not violate the Switendick criterion which would explain for D to occupy both types of interstitials.

The HEA exhibits very slow kinetics without prior activation procedure [68]. For desorption, high temperature is required. TDS measurement by Sahlberg et al. [60] showed the desorption starts at 200 °C with max. peak at 400 °C and at 500 °C H is almost completely desorbed. Complete reversibility of hydrogen desorption after 1 h at 500 °C was also confirmed by Karlsson et al. [31]. The phase transition to the hydride phase start already at 0.1 bar H (for T around 300 °C) and it reported to be a one-step reaction. However, to reach max. H capacity, higher pressure is required (> 50 bar H). For complete desorption, hydride needs to be heated up to 500 °C. Both studies conducted hydrogen cycling experiments consisting of 5 absorption/desorption cycles. Karlsson et al. [31] reported that the material is stable under cycling with slight decrease of c/a and increase of unit cell volume. These findings are different from [60], where they found for the material to separate into two BCC phases with slightly different lattice parameter. The difference in obtained results could be due to different desorption technique. [60] heated up the sample slightly below 600 °C while Karlsson et al. [31] kept

the temperature at 500 °C during cycling. From the phase-temperature diagram and observed single BCC phase in TiVZrHfNb it is evident that at room T the alloy is metastable (stabilized by very slow kinetics). Thus, increasing temperature above 500 °C during [60] desorption experiment which could promote separation of the observed BCC phases after desorption.

1.3. Problem statement

For now, it is still unclear which factors actually affect the HEAs hydrogen kinetics and thermodynamic properties without affecting hydrogen capacity of a hydride. Results from experimental studies indicate a relation between storage capacity and kinetics to be inversely proportional; materials with high storage capacity show slow absorption rate while materials with fast kinetics show poor storage capacity. This relationship between storage capacity and kinetics is not yet clear and should be further explored to uncover factors affecting those two properties. H diffusivity is one of the intrinsic properties of a storage material that governs H absorption kinetics after H penetrates through a surface barrier. To date, determination of hydrogen diffusivity in HEAs for H storage applications has not been done. Most of the research is experimental based using partial substitution approach to observe and compare changes in H properties between different chemical compositions of alloys. However, such approach with numerous possible combinations of different HEA compositions and other external parameters that influence the final properties (e.g. sample initial state, hydrogenation parameters), can be time extensive and difficult to interpreted. Apart from the complexity to find a clear relation between H properties and various parameters, the experimental methods have limitations on quantification of how H interacts with the alloying elements at atomic scale. Experimental methods in combination with first principles simulations can provide deeper understanding of material properties at atomic scale. However, only few studies carried out a theoretical investigation of HEA H storage properties. Therefore, more theoretical based research is needed to gain better understanding on how factors, such as interstitial volume and elemental environment, relate to H movement and preferential occupation within the alloy on atomistic scale.

1.4. Research objective and approach

The motivation behind the project is to gain more fundamental understanding of hydrogen-metal interactions in HEAs, more specifically H diffusivity as a rate limiting step of hydrogenation kinetics. The main objective of this work is to investigate H diffusivity in TiVZrHfNb and the influence of H concentration on H diffusivity. The objective will be achieved by:

- **determining the value of H diffusivity in TiVZrNbHf**
- **observing the effect of H concentration on the H diffusivity in TiVZrNbHf**
- **analyzing a type of interstitial sites the H prefers to occupy in TiVZrNbHf at different H concentration**

Experimental is a better representation of reality, as simulations approximate to the real world. The point of the simulation is to complement experimental observations to compare obtained values of H diffusion and to gain insight on H movement on an atomic-scale, as experimental gives only data on a macro scale. Simulation results have the potential to help explaining the underlying mechanisms for slow absorption kinetics that can be otherwise difficult to obtain from the experiments. The validity of the simulation can be confirmed by comparing its results to the experimental data. Representative simulation findings can be then applied to predict H storage properties in HEAs with different composition.

2

Methodology

The chapter describes in details steps and techniques available to theoretically and experimentally study hydrogen interaction with equimolar TiVZrNbHf. The first part details sample preparation for the experiments which includes synthesis and characterization procedures. The second part describes the experimental procedures and techniques used for electrochemical charging and for detection of the amount of absorbed H. The third part details procedure and used settings for molecular dynamic (MD) simulation. All of the simulations were run with Vienna ab-initio simulation package (VASP) to first, perform optimization of SQS supercell (BCC & FCC) and then MD simulation of H. Processing the obtained simulation data was done with Matlab.

2.1. Sample preparation and characterization

The studied $Ti_{20}V_{20}Zr_{20}Nb_{20}Hf_{20}$ was prepared with high purity raw materials (Alfa Aesar). Table 2.1 contains detailed specifications of the raw materials with T_m and calculated weights of each elements for making 2.5 g samples. Raw material was weighted to ~1 mg precision for as accurate equimolar composition as possible.

Table 2.1: Material specifications, melting T of elements and calculated weights.

Element	**Purity [%]**	**Shape**	**Size [mm]**	**T_m [°C]**	**2.5 g sample [g]**
Ti	99.99	granules	/	1668	0.259
V	99.7	granules	1-3	1910	0.276
Zr	99.8	granules	1-3	1855	0.494
Nb	99.9	granules	2-10	2477	0.503
Hf	99.7	crystal bar milled chips	/	2233	0.967

For this project arc melting method was used for synthesis of TiVZrNbHf alloy. The method is one of the most frequent choice for HEAs synthesis in the literature. Temperatures can reach up to 3000 °C during melting, enough to melt most of the metals. Another advantages of the technique are ability to produce small samples (using minimum amount of material, < 5 g) and among melting techniques arc melting produces the samples with the highest purity and lower amount of porosity. It is also time-saving since there is no need for ball milling as for powder sintering methods. However, the disadvantage of the method is uncontrolled cooling rate which can cause segregation [2, 18, 47]. The studies on TiVZrNbHf HEA published thus far [19, 20, 31, 53, 68] do not provide sufficient details on the melting settings to achieve comparable samples. Therefore, the starting parameters are based on the Campos et al. [7] study. Several iteration to the arc-melting settings were done before obtaining samples homogenized and with the chemical composition close to the initial (within ± 5 at.%). For a sufficient melting of all elements the needed current was found to be 160 A. Table 2.2 contains arc-melting parameters of the three best obtained samples, later used for experiments. The synthesis was conducted with the arc melting unit at the Reactor institute Delft (Figure 2.1).

Table 2.2: Parameters of arc-melting sample preparation.

Sample	**Melting time [min[**	**Remelts**	Ti-getter	**Sample loss [%[**	**Comments**
S6	1	5	yes	0.36	1. melt - pulsing 160 A
S8	1	4	no	0.35	1. and 2. melt at 50 A, then continue with 160 A
S9	1	6	no	0.22	1. melt - 20 A, 2. melt - 50 A, 3. melt - 100 A, 4.-5. melt - 160 A, 6. melt - 50 A

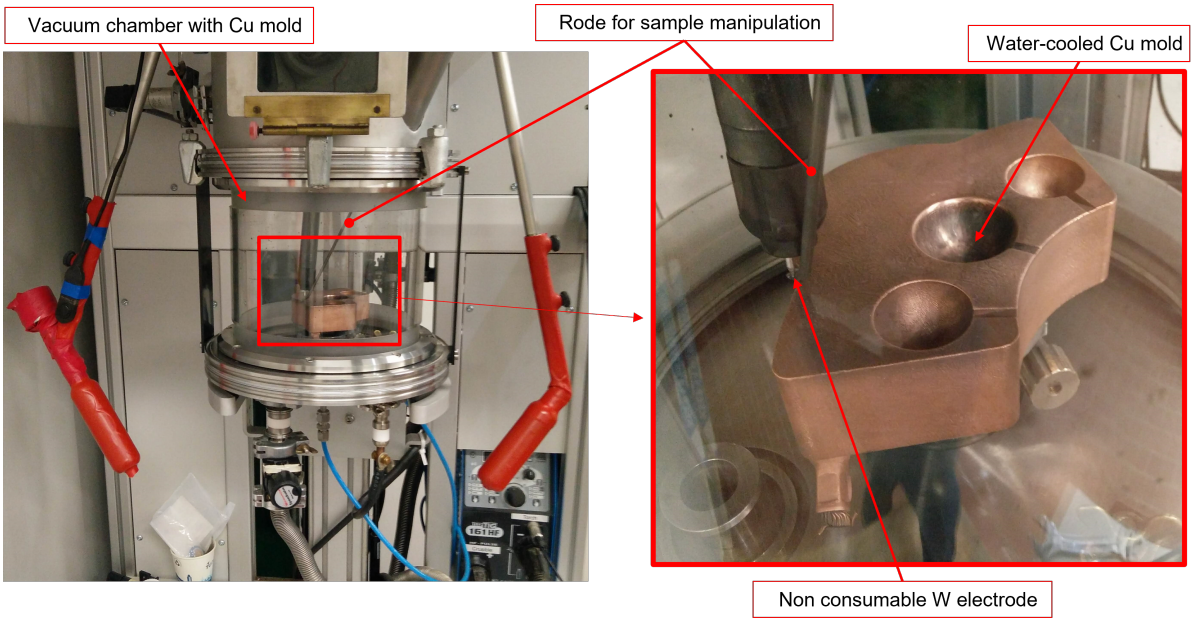

Figure 2.1: Arc melting unit for the sample synthesis.

Prior to melting, the elements with higher T_m were placed on the side of the Cu mold in order to melt those elements first, which helped to melt the lower melting elements underneath. Vacuum pump ran over night to ensure a stable vacuum of ~3×10^{-6} mbar. The chamber was flushed trice with Ar of high purity. The Ar pressure was about 500 mbar. For some of the samples Ti getter was melted prior to melting the alloy to see if Ti getter is needed to prevent oxidation of the samples. However, there was no noticeable difference between samples with and without the Ti getter. In order to prevent excessive splashing of the material, two approaches were used: slowly increasing the current and pulsing. Comments in Table 2.2 describe how those two approaches were applied. Pulsing showed to have less splashing of the material than slow increase of the current. However, non of the approaches prevent material splashing and some of the material ended up outside the mold. Therefore, after the first melt was completed, the chamber had to be opened to collect the splashed material. The chamber was vacuumed again till it reached ~3×10^{-5} mbar (~2 h vacuuming time) and flushed trice with Ar. After the material formed a droplet, there was no more splashing. Before each melt, the samples were flipped to ensure homogeneous distribution of all elements.

Obtained samples were then cut in two different directions to reveal the microstructure (Figure 2.2): The first cross section was cut perpendicular to the Cu mold, further referred to as vertical cross section and the second cut was parallel to the mold, further referred to as horizontal cross section (Figure 2.2 b) and c) respectively). Cutting the samples was done with a low speed cutter using gravity fed force for minimal deformation on the samples.

After that, the cut samples were prepared for chemical analysis using 320 to 4000 grit SiC paper, 1 µm and 0.25 µm Al_2O_3 (OP-S Struers) polishing liquid. To clean the samples from any leftover polishing particles, the samples were placed in an beaker filled with iso-propanol and put into ultrasonic bath for approx. 15 min.

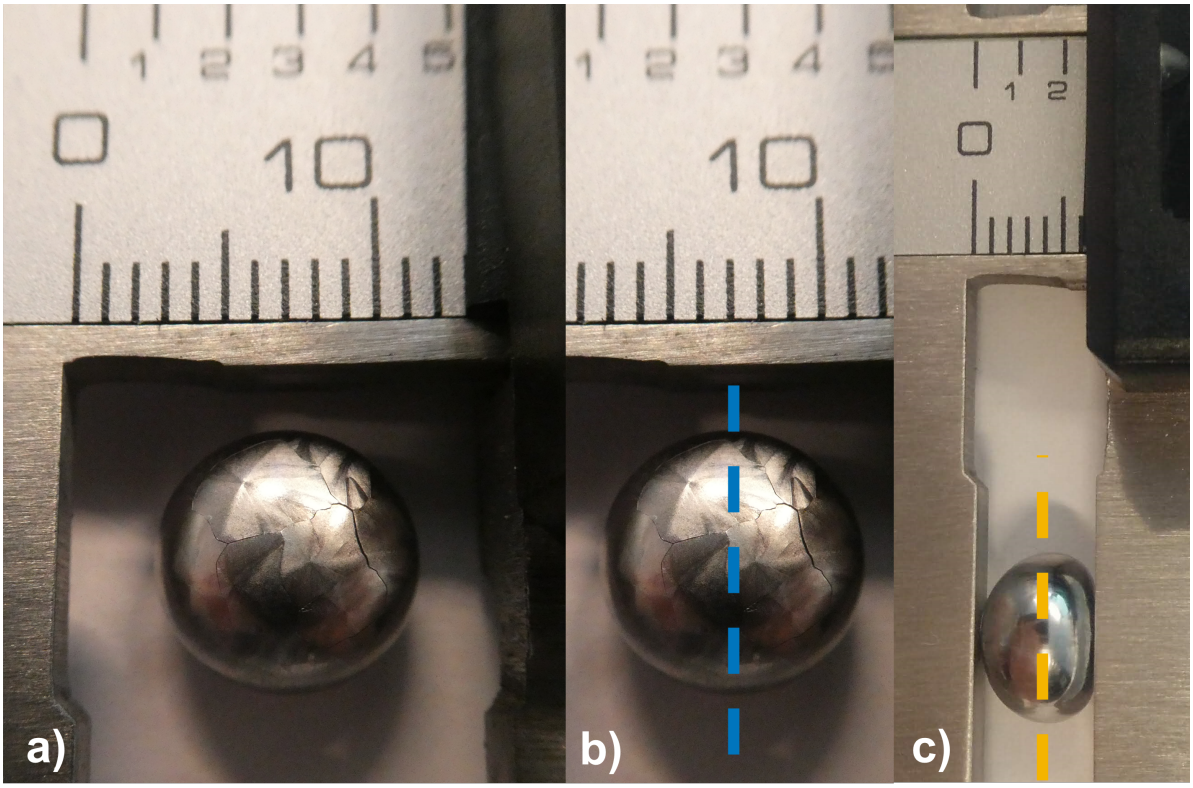

Figure 2.2: As-cast sample - a) droplet shape; b) blue dashed line - vertical and c) orange dashed line - horizontal cross sections.

For electrochemical charging, samples were prepared by exposing horizontal cross section of the sample since it has more uniform microstructure compared to the vertical, thus minimize the extend of microstructural influence on charging conditions. The samples were first embedded in an acrylic non-conductive cold mounting resin (ClaroCit Kit, Struers). Afterwards, the embedded samples were sanded to the desired depth using the coarse 80 grit SiC paper and continue with the procedure as described in previous paragraph.

Evaluation of the condition and quality of as-cast samples was done using standard characterization techniques (XRD, EDS, XRF and SEM). Microstructure and chemical composition of the as-cast samples were analyzed with scanning electron microscopy (SEM) JEOL JSM 6500F using backscatter electron and energy dispersive spectroscopy (EDS) detectors. SEM images were obtain using backscatter electrons (BSE) at 20 kV acceleration voltage and 10 mm working distance.

EDS mapping was used to verify the elemental distribution of the samples. The exposure time was set to 30 min with the probe current fixed to the value where ~15 000 counts/sec were reached. The end mapping results were converted from wt.% to at.%. Line EDS for measuring the variation between different zones was set to 1 min per spot. For comparison to EDS results, additional measurements were performed with a Panalytical Axios Max Wavelength Dispersive X-Ray Fluorescence (WD-XRF) spectrometer and data evaluation was done with SuperQ5.0i/Omnian software.

The crystal structure was determined by X-ray diffraction (XRD) analysis using a Bruker D8 Discover diffractometer and Eiger-2 500k 2D-detector with Cu Kα radiation (λ = 1.54 Å). The scanning was done 10-110° 2θ with set step size 0.04° and time per step 2 s. All the XRD measurements were done at room temperature on the bulk samples.

2.2. Electrochemical hydrogen charging procedure

The experimental measurements were carried out at room temperature in a standard three electrodes cell made from non-reactive acrylic material with the opening of 3.9 mm diameter. A double junction $Ag/AgCl_{sat}$ electrode (+0.197 V vs. SHE) served as a reference (RE), a platinum foil (99.95 %, 15×15×0.5 mm, GoodFellow) as a counter (CE), and the HEA as working electrode (WE). All potentials are reported against $Ag/AgCl_{sat}$ (4M KCl). Due to safety constrains, 1M KOH (56 g mixed with 1 L of demi H_2O) electrolytic solution was used.

Figure 2.3 shows the experimental setup. The measurements were performed with Bio-Logic VSP-300 (EC-Lab® software) potentiostat.

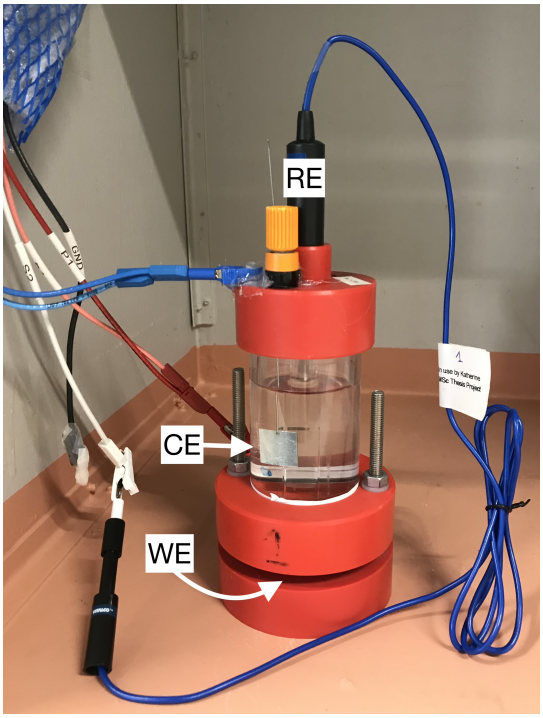

Figure 2.3: Final look of prepared sample for electrochemical H charging experiments.

The preparation of sample surface was as described in the previous section 2.1. A Cu tape was placed on the backside of the sample to insure the electrical connection with the potentiostat. The exposed area was marked by cutting a 3 mm hole in chemically resistant tape and placing it over the sample, as shown in Figure 2.4. This also provided fixed charging area, since the area can vary, depending on tightening of the bolts. For all the measurements, absolute current was normalized to the geometric area. As shown in the Figure 2.3 the sample was placed between the plates of the cell and secured with tightening of the bolts.

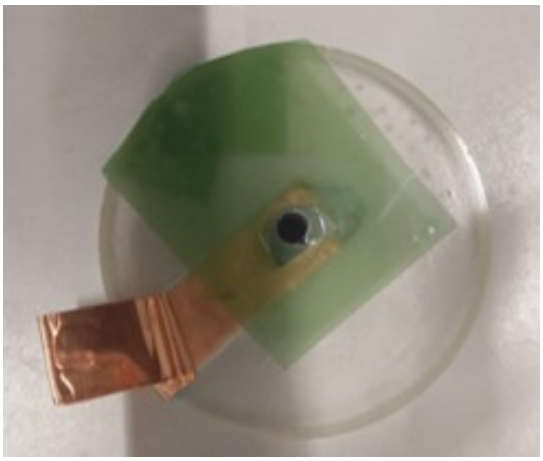

Figure 2.4: Final look of prepared sample for electrochemical H charging experiments.

Since $Ag/AgCl_{sat}$ RE can be unstable in basic solutions it is important to check stability of the electrode before and after the experiment[1]. The calibration procedure was as follows:

[1] The difference between the electrodes was always below 1 mV.

1. Filling solution of 4M KCl was renewed before calibration and the RE was left to stabilized for about an hour.
2. The RE potential was measured against the Ag/AgCl (3M KCl) electrode used only for the calibration purposes.
3. After the electrochemical experiments, the RE potential was measured again against the Ag/AgCl (3M KCl) electrode after stabilizing for about an hour.

The experimental charging procedure consist of two different approaches. In the first approach, one run consist of three consecutive steps, using electrochemical techniques:

1. Cyclic Voltammetry (CV): obtaining baseline (pre-charging conditions)
2. Chronoamperometry (CA): applying fix potential to the sample (charging H to the sample)
3. Cyclic Voltammetry (CV): detection[2] of desorbed H as a new peak in the 1st scan; additional scans after are used to determine the state compared to the baseline

Several iteration of the settings were done in the first approach. In Table 2.3, setting used for each run are presented. The potential range was later changed to avoid the material oxidation region. Apart from varying CA charging time and potential, the variation of CV scan rate was also tested to see the effect on the final results. However, the scan rate showed no significant effect on the results and therefore, is not discussed further.

Table 2.3: CV and CA settings used in each run of the first approach for H charging; potential values are expressed against $Ag/AgCl_{sat}$.

	CV		CA	
run	potential range [V]	sweep rate [mV/s]	potential [V]	time [h]
1	-1.7 to 0.6	50	-1.7	1
2		10	-1.5	1
3				6
4		20		1
5				6
6		50		1
7				6
8	-1.5 to 0.2	20	-1.7	1
9			-1.6	
10			-1.5	

The second approach consist of CA-only (to avoid any surface passivation during CV). The applied charging potential was set to -1.55 V and three charging time were 72, 168 and 450 h. After the charging, the sample was removed and immediately analyzed by XRD for detection of structural changes caused by absorbed H.

[2]Only H that electrochemically recombines (exchange of electrons) can be detected as a current response.

2.3. Computational methods

For ab initio molecular dynamic (AIMD) calculations a simulation cell for the random TiVZrNbHf solid solution was constructed. From the research thus far the TiVZrNbHf has BCC crystal structure whose hydride has been reported to form BCT or FCC. For simplification, the hydride structure in the present work is FCC. To simulate a random solid solution the special quasirandom structure method (SQS) was used to create the supercells. The SQS size of the simulation cells needs to be large enough to have good representation of random solid solution (unique local chemical environment) but small enough for time efficiency. Both BCC and FCC supercells consist of 5x5x5 primitive cells, containing 125 metal atoms to obtain an equiatomic composition. The decision on the minimum number of atoms needed for a representative SQS is based on the number of unique combinations of the 1st and 2nd nearest neighboring metal pairs.

All simulations based on Density-Functional-Theory (DFT) were done with Vienna Ab-initio Simulation Package (VASP) using the Perdew-Burke-Ernzerhof (PBE) generalized gradient approximation (GGA) for the exchange and correlation energy. The ion-electron interactions were based on the projector augmented wave (PAW) method. For expansion of electronic wave functions the recommended Gamma-centered k-points grid was used (autogenerated).

The first step was to relax the generated SQS-cells without H by allowing the supercell's volume and position of initial atoms to change while keeping the initial structure fixed. The convergence criterion for acting forces was set to 0.001 eV/Å and the total energy tolerance was set to 0.0001 eV. The energy cutoff for system relaxation was set to 400 eV and 380 eV for BCC and FCC, respectively.

For ab initio molecular dynamic (AIMD) runs, a different number of H atoms (Table 2.4) were placed in interstitial sites of the obtained relaxed BCC and FCC. The selection of the starting H interstitial sites is based on the sites where the acting force on H in the cell was the lowest. For all MD calculations the energy cutoff was set to 200 eV and the total energy tolerance was increased to 0.00001 eV. The temperature was approximately constant for each MD run and thermal equilibration was controlled by Nosé-Hoover thermostat with the NVT (number of atoms, volume and temperature) canonical ensemble. During the runs all atoms of the system were allowed to move while the cell's volume was fixed. A time step dt was set to record a position of each particle every 0.75 fs and gives a good compromise between time efficiency and temperature stability where one oscillation movement of H should be described with about 40 time steps.

Characterization of particle movement inside the simulation cell can be determined by calculating mean square displacements (MSD) for a time interval Δt:

$$\mathrm{MSD}(\Delta t) = \left\langle |\vec{r}(t+\Delta t) - \vec{r}(t)|^2 \right\rangle = \frac{1}{N \cdot m} \sum_{i=1}^{N} \sum_{j=1}^{m} \left| \vec{r}_i(t_j + \Delta t) - \vec{r}_i(t_j) \right|^2 \tag{2.1}$$

where $r(t)$ is a position of a particle at a time step t and $r(t+\Delta t)$ is a new position of the particle after Δt. The brackets $\langle\rangle$ represent an ensemble average over the total number of time intervals m.

The MSD relates to the diffusion coefficient D as

$$\mathrm{MSD} = 2\, d\, D\, \Delta t \tag{2.2}$$

for d is dimension, D is diffusivity for a time interval Δt. The diffusivity obtained from Equation 2.2 is valid only when the MSD shows a linear trend with Δt. Therefore, values of MSD were processed by the simple linear regression [3]. After obtaining H diffusivities D_H from MSD at various temperatures, activation energy (E_a) and pre-exponential factor (D_0) can be estimated from Arrhenius equation

$$D_H = D_0 \exp\left(-\frac{E_a}{k_B\, T}\right) \tag{2.3}$$

where k_B is Boltzmann's constant ($= 8.62 \cdot 10^{-5}\, eV/K$). Transforming Equation 2.3 into a logarithmic form and by fitting the regression line to the logarithmic values of diffusivities, one can obtain E_a and D_0 from the fitted regression line equation as the slope and intercept, respectively. The goodness of the fit was determined by coefficient of determination R^2. For a good estimation of E_a and D_0, D_H needs to be obtained for at least three different temperatures.

In this study, the selected temperature range (Table 2.4) is based on the temperature (~ 573 K) that was experimentally found by Karlsson et al. [31] for the TiVZrNbHf to form the hydride-phase. From the point of

the time efficiency the selected temperature range is higher to allow H to diffuse longer distances in shorter time.

The estimation of the needed time frame of the simulation was defined by checking the time that it takes for H to cover the minimum average distance of double the lattice parameter. This was done by first running an initial simulation for the BCC structure with 25 H. After reaching the set criteria, the time was extrapolated to the rest of the cases. The number of analyzed steps was larger for BCC with 25 H to decrease the standard error of MSD due to the lower number of H atoms.

From the study by Sleiman and Huot [68] the transition from BCC to hydride phase (FCC) occurs when the concentration reaches ~1.1 H/M. The maximum hydrogen capacity was reported to be at 2.5 H/M [60]. Therefore, the range of H concentration selected for BCC is 0.2 - 1.4 H/M and for FCC is 1.4 - 2.4 H/M.

Table 2.4: Overview of the MD runs for BCC and FCC; H_x is the total number of hydrogen atoms in the supercell, t is a total simulation run time and τ is a time interval taken from the end part of the total simulation run time (used for analysis).

T	**Cell**	**H_x**	***t***		***τ***
[K]			steps	[ps]	steps
673	BCC	25	90396	68	48000
773			90051	68	
873			100000	75	
973			100000	75	
773		100	60000	45	28000
873			60000	45	
973			60000	45	
973		175	30000	23	
773	FCC	175	77527	58	
873			73891	55	
973			72998	55	
773		250	50000	38	
873			75100	56	
973			74300	56	
773		300	75205	56	
873			82432	62	
973			74407	56	

Additional runs for FCC were done at 873 K with 220 - 290 H[3] to obtain more information about the effect of H concentration on D_H. For each run the number of H was increased by 10. More details about the MD simulation runs are presented in Table 2.5.

Table 2.5: Overview of the additional MD runs for FCC; H_x is the total number of hydrogen atoms in the supercell, t is a total simulation run time and τ is a time interval taken from the end part of the total simulation run time (used for analysis).

T	**H_x**	**Cell**	***t***		***τ***
[K]			steps	[ps]	steps
973	220	FCC	18886	14	16886
	230		13630	10	11630
	240		13199	10	11199
	260		12517	9	10517
	270		12291	9	10291
	280		11351	9	9351
	290		11149	8	9149

[3] Excluding the primary MD calculation done with 175, 250 and 300 H atoms.

3

Results and Discussion

3.1. As-cast sample analysis

The analyzed as-cast samples have chemical composition within ±3 at.% of the initial values. The chemical composition measurements are presented in Table 3.1 and the EDS measured areas are indicated in Figure 3.1. Compositional deviation between XRF and EDS results can be due to the way the systems were calibrated. From the Figure 3.3 the elements are on average homogeneously distributed; more noticeable segregation can be observed for V and Nb in the region with coarser dendrites.

The morphology of the as-cast samples is mostly dendritic. From a horizontal cross section (Figure a) 3.2) boundaries of dendritic clusters can be observed while for vertical cross section (Figure b) 3.2) the dendrites have strong orientation in the solidification direction. In the center of a sample where the cooling rate is the slowest, dendritic branches are thicker and without preferential orientation. The morphology between the samples slightly varies due to different settings of arc-melting (details in the section Methodology, Table 2.2).

A degree of chemical variation between dendritic and interdendritic areas was further analyzed with line EDS. From the results (Table 3.2 there is slight variation in chemical composition between light (dendritic) and dark (interdendritic) regions (Figure 3.4). The amount of Ti is constant in both regions. In the dark region V and Zr increase at similar rate while the amount of Hf and Nb decreases. The most noticeable difference between the regions is in the amount of V and Nb. This chemical variation between the regions has been found to be slightly different compared to the research on the TiVZrHfNb alloy [19, 68]. However, sample preparation with arc-melting is not very well controlled process; loss of some material during splattering that occurs in the first arc-melting and uncontrolled solidification rate can contribute to variation in the end result of the chemical composition.

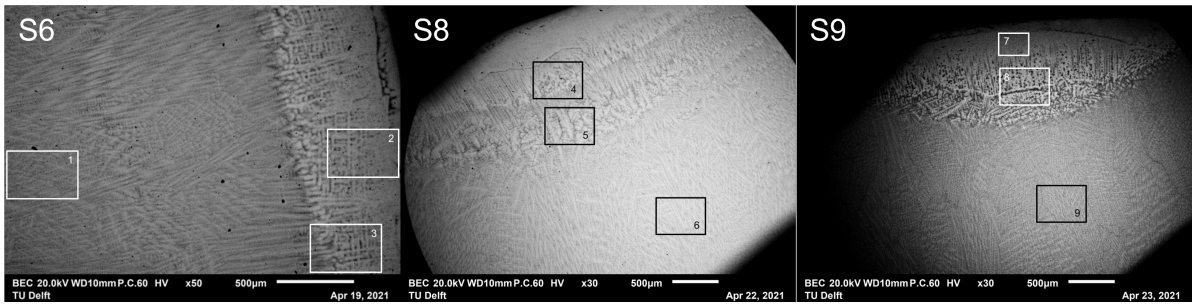

Figure 3.1: SEM images of the analyzed samples recorded with BSE. The squares mark the areas measured by EDS.

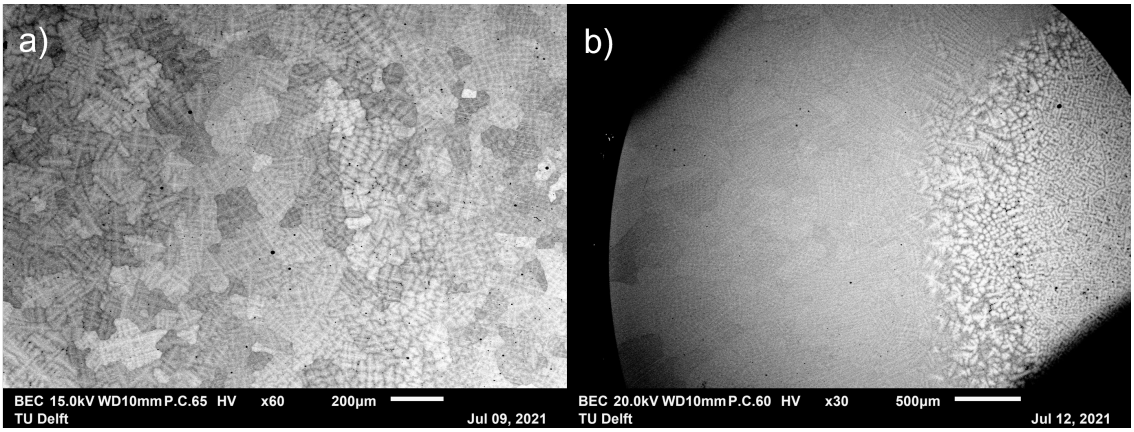

Figure 3.2: SEM-BSE images of as-cast sample a) horizontal (x 60) and b) vertical cross section (x 30).

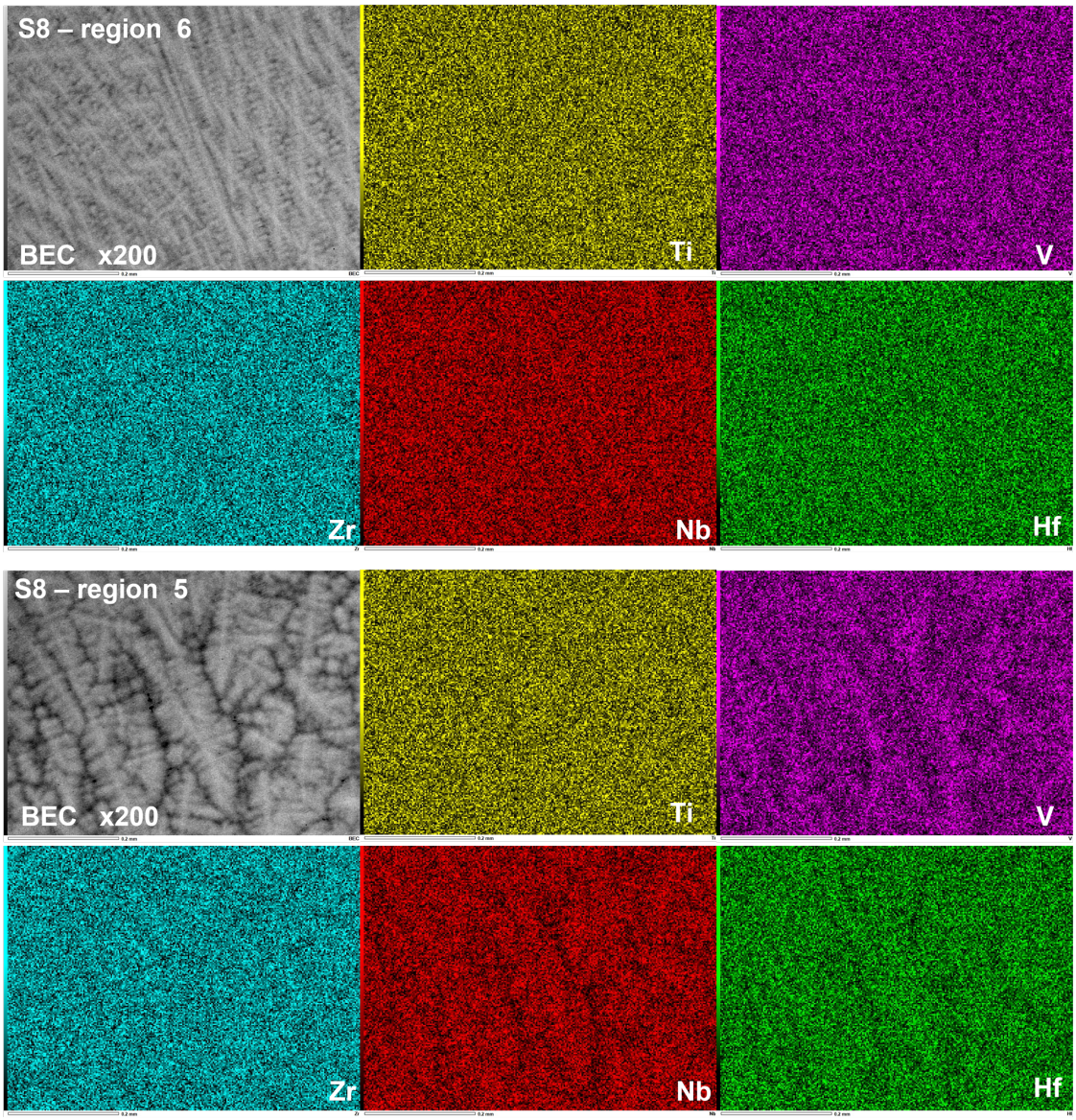

Figure 3.3: Images of elemental distribution obtained with EDS mapping. The measurements of two different areas in the sample S8 where some variation in the distribution is observed.

Table 3.1: Chemical composition (at.%) of the selected as-cast samples analyzed by EDS mapping (regions indicated in 3.1) and XRF.

Sample	Spectrum	Ti	V	Zr	Nb	Hf
S6	1	20.77	20.36	18.69	19.64	20.55
	2	20.89	20.08	18.48	20.04	20.50
	3	20.84	19.89	18.48	20.14	20.65
	XRF	21.70	22.11	19.80	19.43	16.96
S8	4	20.79	20.73	18.87	19.45	20.17
	5	20.80	21.53	19.07	18.79	19.81
	6	20.86	21.37	18.99	18.96	19.82
	XRF	23.53	20.01	19.22	19.59	17.65
S9	7	20.84	21.10	18.87	19.19	20.01
	8	20.88	21.01	18.83	19.24	20.04
	9	20.89	21.51	18.96	18.81	19.84
	XRF	22.30	20.79	19.36	19.53	18.03

Table 3.2: Chemical composition (at%) of average, dendritic and interdendritic region analyzed by line EDS, indicated in 3.4.

Spectrum	Ti	V	Zr	Nb	Hf
Average	20.75	23.06	19.94	16.86	19.38
Interdendritic (1)	19.83	28.16	24.23	10.94	16.83
Dendritic (2)	21.47	18.56	17.60	21.43	20.94

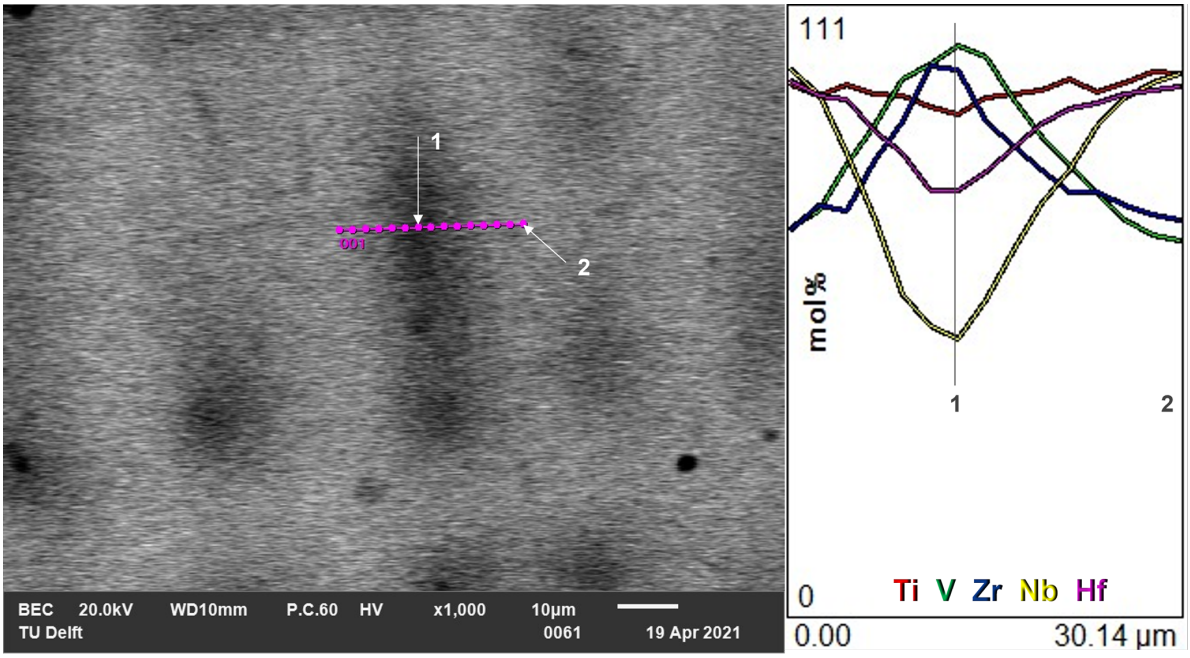

Figure 3.4: Line EDS analysis of (1) interdendritic and (2) dendritic region of as-cast sample as indication of some variation in chemical composition.

XRD patterns confirmed for the TiNbZrHfV to be cubic (BCC) with lattice parameter of 3.37 ± 0.008 Å. The value of the lattice parameter is similar to the values obtained in previous reported studies [19, 53, 60, 68]. Figure 3.5 shows the measured XRD patterns, after background subtraction and small displacement correction. The colored sticks give the peak positions and intensities of the present crystalline phases, using the ICDD pdf4 database. The samples have structure with lattice parameters close to that of HfZrNb3. For a better display of the small peaks, the intensity scale is square root. The diffraction patterns show some variation in peak intensity between the samples; for the sample S6 mostly peaks (110) and (211) were detected while

for the samples S8 and S9 more peaks were detected with the stronger peak (110). This indicates preference in grain orientation and variation of grain size.

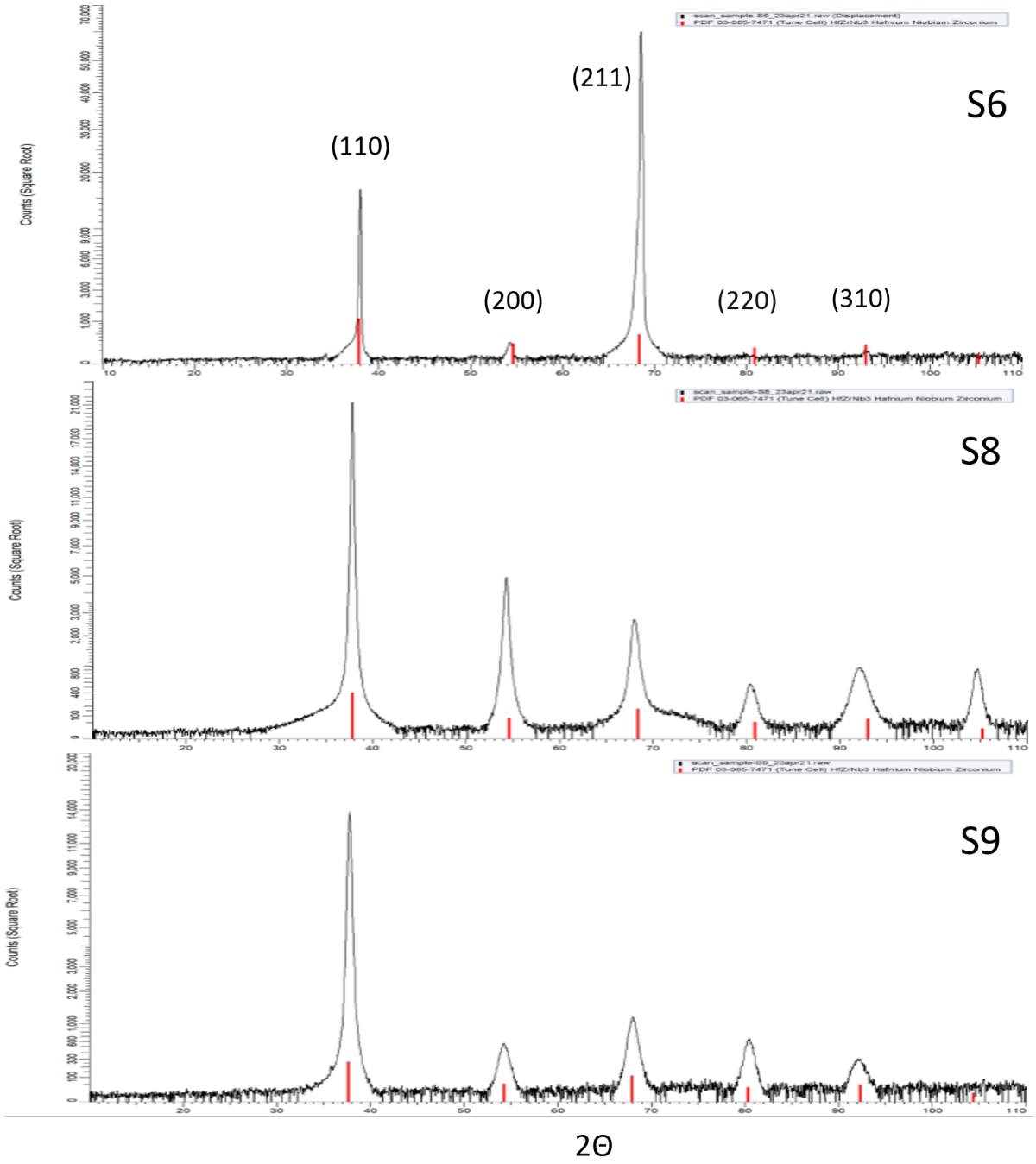

Figure 3.5: XRD patterns for sample S6 (top), S8 (middle) and S9 (bottom). The red sticks give the peak positions and intensities of the possibly present crystalline phases, using the ICDD pdf4 database; intensity scale is square root.

3.2. Electrochemical hydrogen charging results

For the purpose of charging hydrogen into the HEA, the electrochemical charging method (chronoamperometry) was selected as safer and more accessible option compared to hydrogen gas charging method. However, no research of electrochemical properties of the TiVZrNbHf HEA has been conducted thus far. Therefore, starting charging procedure followed procedures found in literature. From the literature there are several factors which have an effect on hydration process that have to be taken into account [57]:

1. Thermodynamics - depending on an applied charging potential and pH of a electrolytic solution different electrochemical reaction can occur; regions of the occurring reaction for a material for given pH and charging potential is represented by Pourbaix diagram (Figure 3.6). Due to unknown nature of the TiVZrNbHf, charging values for the selected pH were obtain from Pourbaix diagram for Ti as starting point for the charging experiments. From the diagram it can be seen that for reaching TiH_2 region a high overpotential (~ 0.7 V) is required throughout the whole pH range.

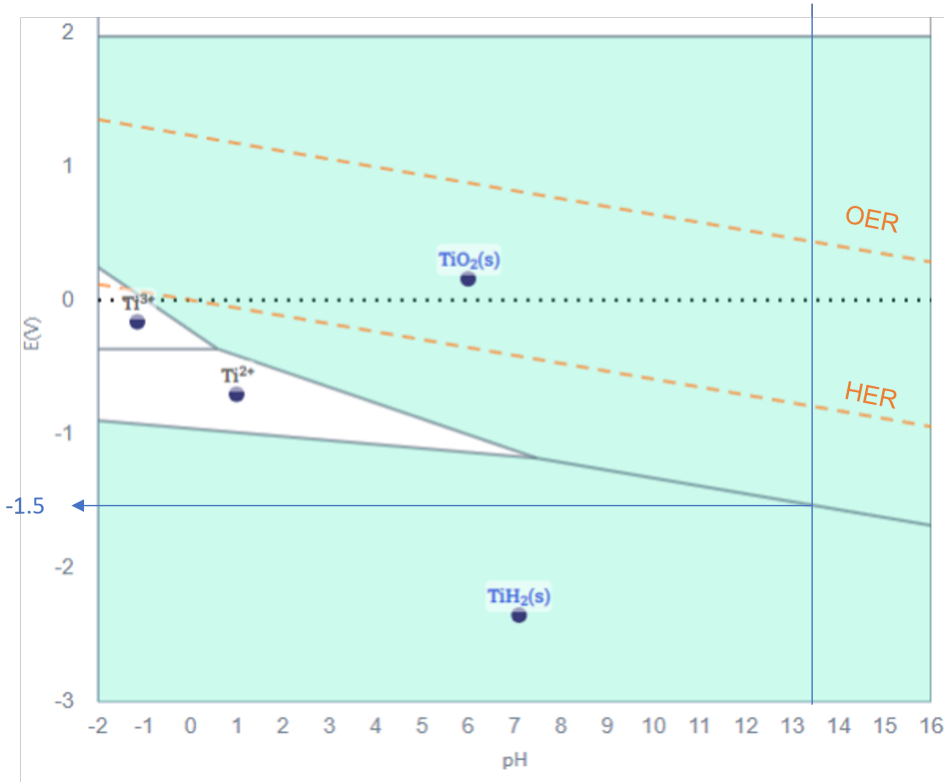

Figure 3.6: Pourbaix diagram for Ti (obtained from materialsproject.org [55]). The blue arrow indicate the charging potential (V vs. SHE) for the selected pH where hydrogenation of Ti starts; the top orange dashed line marks oxygen evolution reaction (OER) and the bottom line marks hydrogen evolution reaction (HER).

2. Kinetics - the following parameters affect the hydride formation through electrochemical hydrogenation process:
   (a) Overpotential - influences the rate of H dissociation; higher the overpotential, easier is for H to dissociate, leading to the higher amount of H and thus faster hydrogenation.
   (b) Charging time - when the H absorption rate is slow, increasing the charging time allows more H to get absorbed
   (c) Solution's pH – the reaction rate for the H sorption is known to be higher in acid than in neutral or basic solutions due to higher concentration of protons in acid; in basic solution H_2O needs to be split first to obtain protons. However, lower pH can cause degradation (corrosion) of a material.
   (d) Surface properties - oxide layer, impurities, surface defect, etc. can change the energy barrier of the surface, affecting the H sorption ability of a material; especially oxygen layer is known to increase the energy of the surface, decreasing H absorption rate.

(e) Charging temperature - increasing the temperature is known to increase the reaction rate; from the research [68] on TiVZrNbHf alloy charged with H gas shows that also activation of absorption occurs faster when charging at higher temperature.

From the thermodynamics perspective it should be possible to charge the HEA with H electrochemically, providing low enough potential for selected pH. However, which metal-electrolyte surface processes [57] will occur during electrochemical charging also depends on duration of exposure, temperature, solution composition, material composition, and other factors. Due to complexity and time limitations of the charging experiment, the focus is on the charging time and overpotential.

3.2.1. Pre-charging conditions

No studies have been conducted on TiVZrNbHf HEA using electrochemical hydrogen charging technique. Therefore, it was necessary to first establish baseline electrochemical response of the alloy prior to charging and relate the behavior to Pourbaix diagram.

CV scans with the potential range from -1.7 V to 0.6 V vs. $Ag/AgCl_{sat}$ at 100 mV/s (Figure (b) 3.7) shows an occurrence of surface passivation. The oxidation peak is only visible for the 1st CV scan and does not appear after further scanning. The exposed sample surface did not show any visible changes due to oxidation. The Ti Pourbaix diagram (Figure 3.6) indicates that above -1.7 V vs. $Ag/AgCl_{sat}$ the material starts to oxidize. However, CV results shows a delayed start of material oxidation at around -0.4 V. The CV results show similar response as Ti [46] (Figure (a) 3.7). Extending the CV potential range to more negative values did not show any noticeable peaks indicating redox reactions.

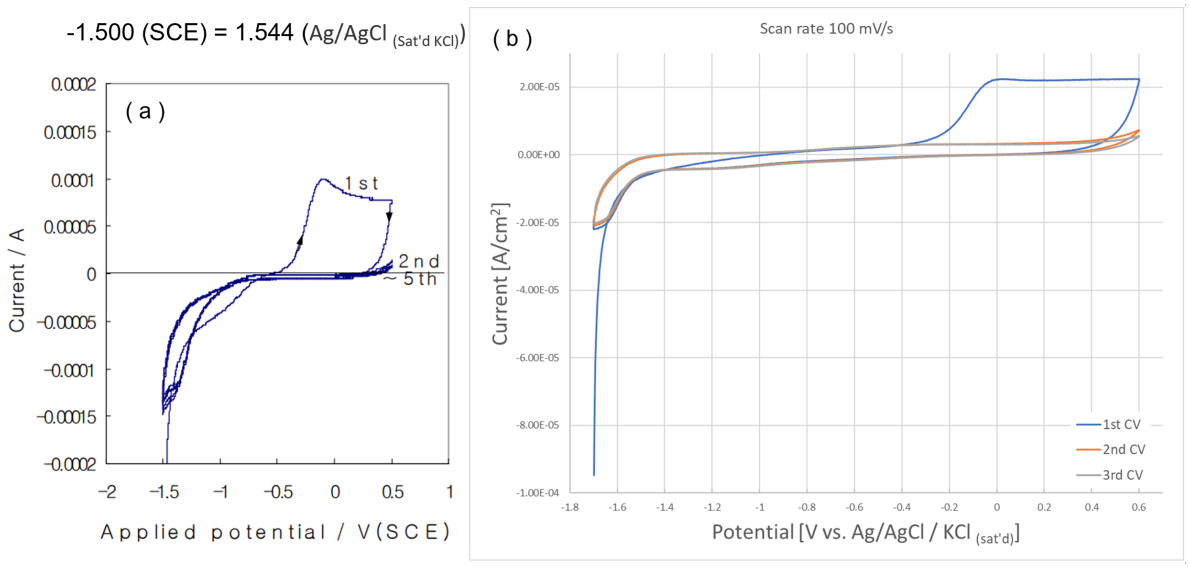

Figure 3.7: Comparison between cyclic voltammograms of (a) Ti [46] and (b) the TiVZrNbHf sample from -1.7 V to 0.6 V vs. $Ag/AgCl_{sat}$ at 100 mV/s; the 1st scan shows irreversible oxidation peak.

3.2.2. Charging results

Increase in charging overpotential (below -1.7 V) produced increased formation of visible H_2 bubbles and rapid increase in cathodic current. For charging at -1.7 V H_2 bubbles could not be detected anymore. However, from the current increase (Figure (a) 3.8) it can be seen that the formation of H_2 still occurs, though at lower rate. The stable current (plateau) values are close to zero for charging > -1.7 V. Since no changes due to H absorption could be detected, it is likely that the steady-state current indicates saturation of the surface (H adsorption and recombination rate are equal).

Figure (b) 3.8 shows voltammograms obtained after charging. From the 1st CV scan it was expected to observe an additional peak due to H oxidation (H desorption). From the voltammograms the peak cannot be seen since the shape of 1st CV looks almost identical to the baseline. The only observable difference between the 1st CV scan and the baseline is the anodic part of the curve with slightly higher current values for the 1st CV scan. Interestingly, by lowering the charging overpotential, the CV anodic current values also decrease

(Figure 3.9). Failing to detect desorbed H could be due to recombination of H chemically. Since electrons are not involved in the chemical recombination reaction, detection of desorbed H is not possible through electrochemical methods such as CV.

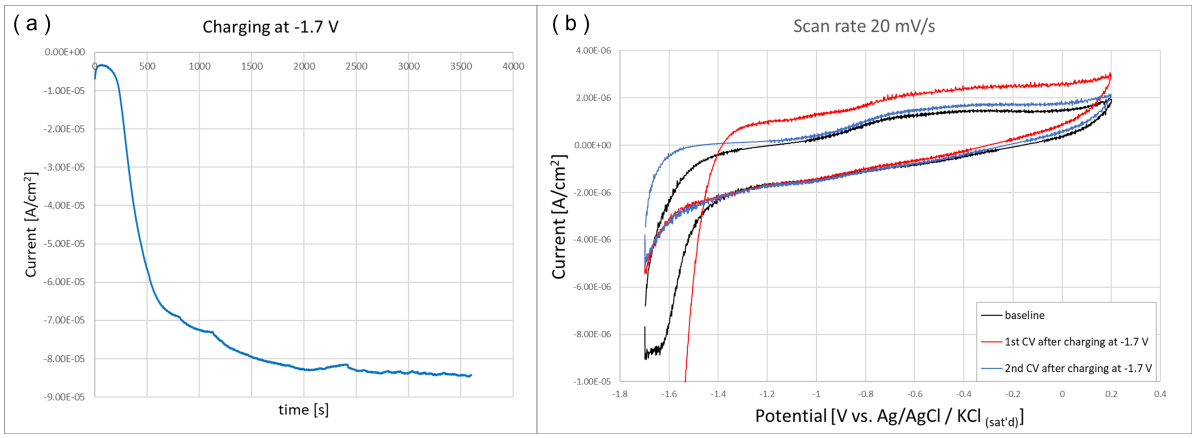

Figure 3.8: Charging results: (a) charging curve at -1.7 V vs $Ag/AgCl_{sat}$ for 1h and (b) CV scans at 20 mV/s before and after charging.

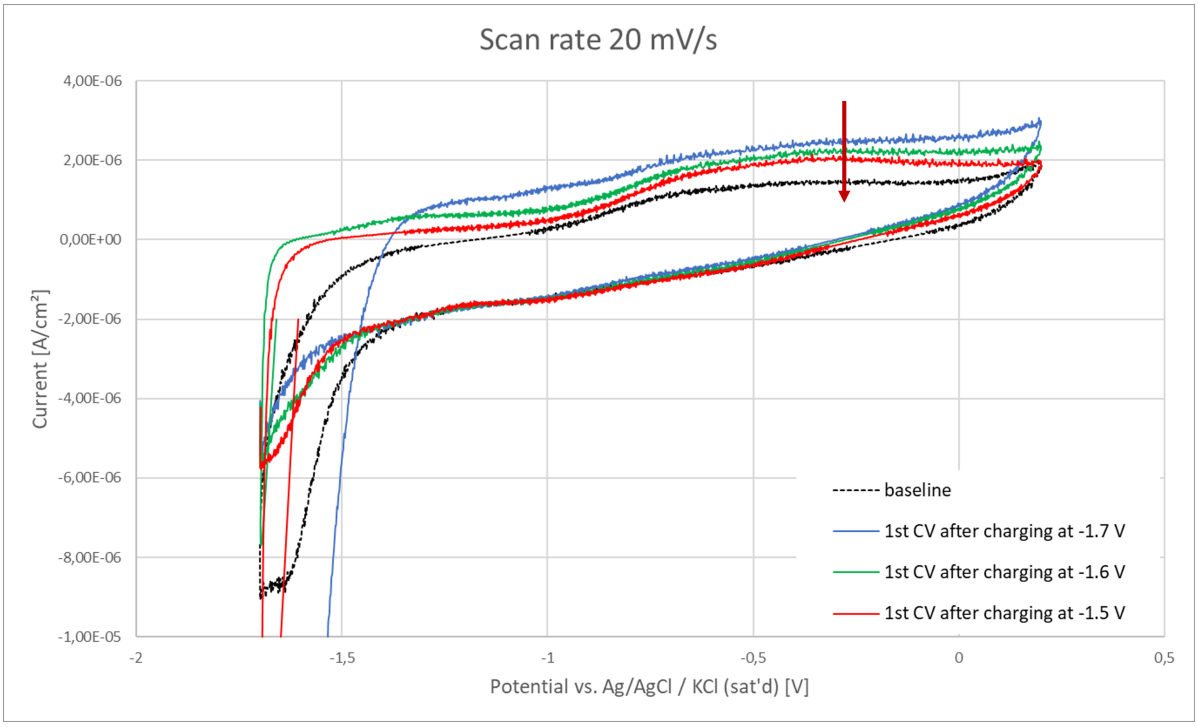

Figure 3.9: Voltammograms obtained after charging for 1 h at different potentials. The arrow indicates decreasing values of anodic part of the curve as set charging potentials are higher.

From the results it is evident that hydrogen evolution reaction (HER) is the predominant process at high overpotentials. For H loading the HER is undesirable since it occurs at a higher rate than the absorption reaction, which limits the amount of adsorbed H for possible absorption. At cathodic overpotentials HER is unavoidable because it occurs in parallel with H absorption reaction. However, which reaction will be predominant mostly depends on the surface reactivity with H. In general, transition metals do not attract H very strongly which means HER is more pronounced than H absorption. Since the TiVZrNbHf consist of transition metals, predominant HER indicates low surface reactivity with H. A use of recombination poison or coating surface with thin Pd layer might limit loss of adsorbed H due to HER during charging at high overpotential needed to reach hydride region. However, the poison effect on the TiVZrNbHf is thus far unknown and should be investigated in future research.

From the pre-charging CV results, the TiVZrNbHf forms irreversible oxidation layer. Therefore, the passive layer that forms during the process of obtaining baseline further decreases surface reactivity with H. This would explain no detection of H desorption peak (Figure (b) 3.8), albeit from oxidation of adsorbed H. Passivated surface can promote anodic processes (adsorption of O/OH and oxidation) to occur simultaneously with cathodic, which hinder H adsorption as well.

Figure 3.10 shows the results obtained for extended time charging without CV scans prior to the charging to avoid formation of passive layer during the scans. The results show current increase after 5 h. The reason for the offset of the current could be formation of the oxides, triggering the HER to occur for the applied potential.

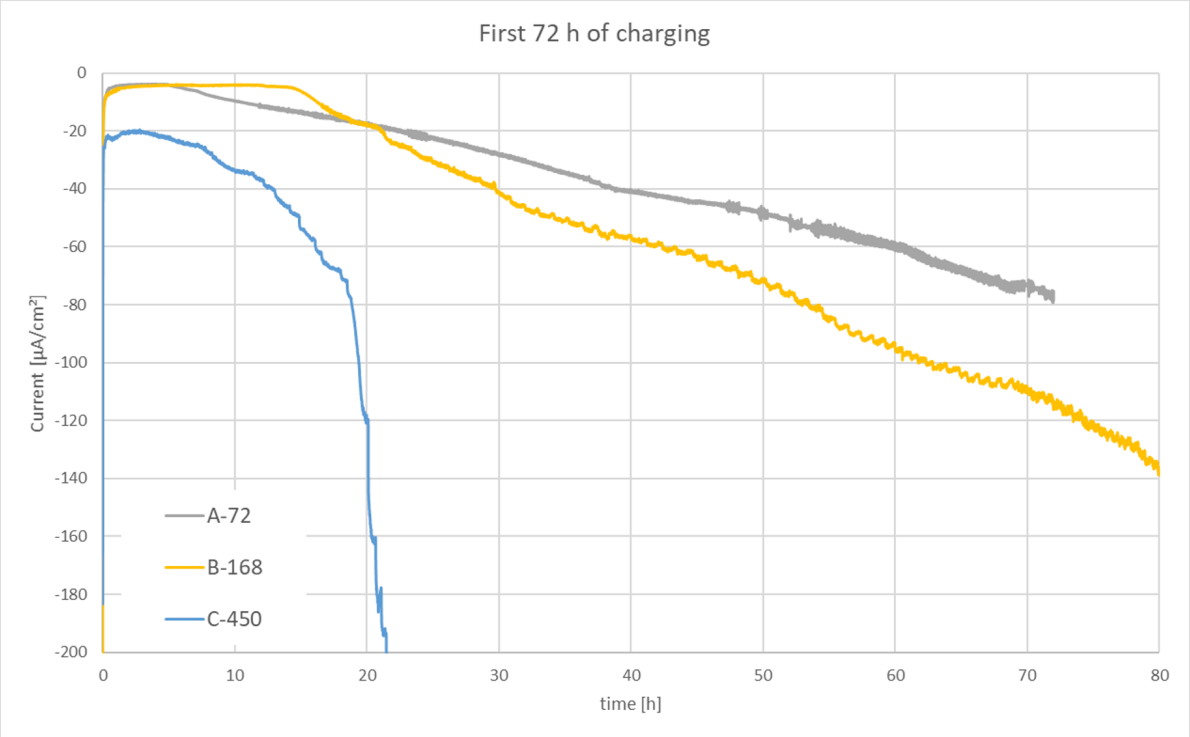

Figure 3.10: CA results (from the first 72 h of charging) from three separate H charging for extended period of time with the applied potential of -1.55 V; A-72, B-168 and C-450 denote charging runs for 72 h, 168 h and 450 h respectively.

Oxygen layer has been shown to have a big impact on H sorption. The extend of oxide influence on the H sorption process depends on the valance state of the surface layer [54, 71]; for low valence surface state the H entry can still be possible provided sufficient charging time to compensate for slower reaction rate. It was expected for the alloy to absorb some amount of H by providing long charging time and charging in a potential region where HER is minimum and the top layer might form suboxides.

A detection of the absorb H was done through XRD measurements as changes to the lattice parameter before and after charging-only. The XRD analysis was conducted right after the charging was complete to prevent any (possible) changes. It is expected to find diffraction peaks for BCT structure (hydride formation) or at least a shift of the diffraction peaks (towards lower angles) due to the expansion of the lattice caused by absorbed H.

Figure 3.11 shows the measured XRD patterns before and after H charging for 72 h. For the sample A-72 (after charging for 72 h) all BCC peaks are visible, whereas in the sample before charging only the (200) and (310) reflections are visible. Since the samples do not have uniformed microstructure (different grain size and preferred orientation) it is possible that the probed area after charging detected some grains with different orientation that were not detected in the previous measurement.

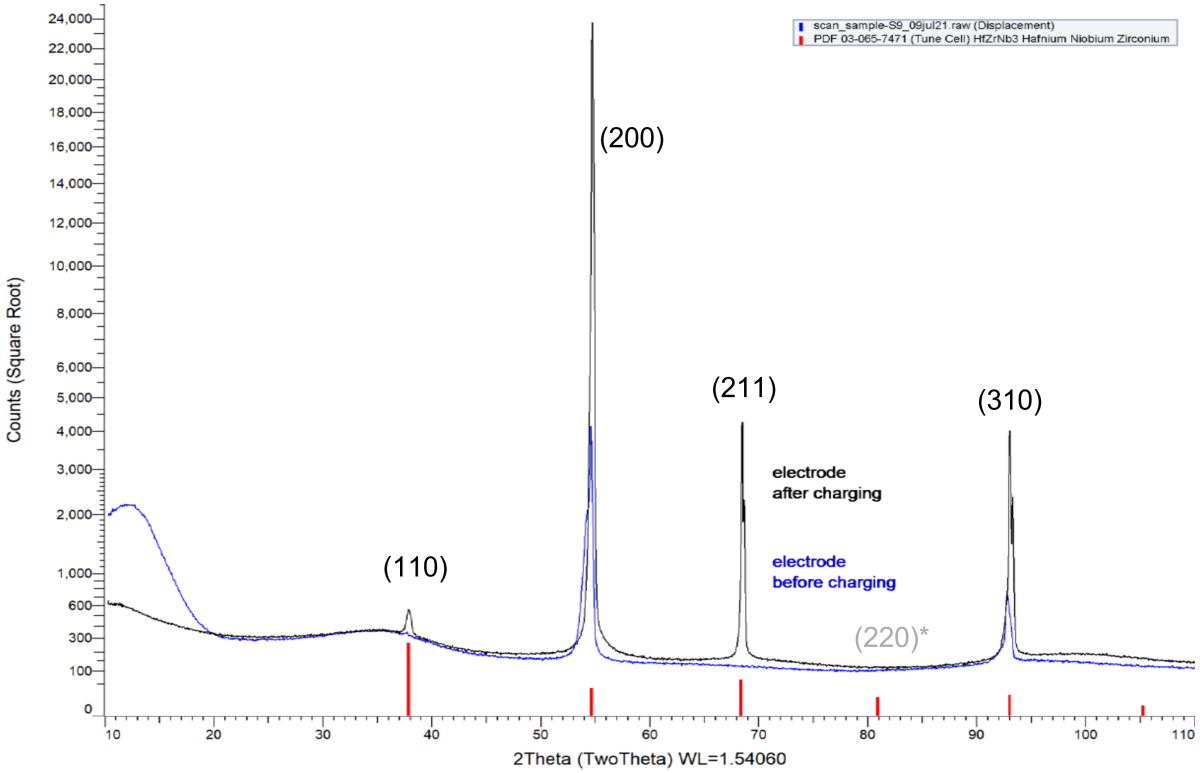

Figure 3.11: XRD patterns of the sample before and after H charging for 72 h; intensity scale is square root.

After charging for 450 h, a black layer formed on the surface (C-450). This layer is also visible on the XRD patterns (Figure 3.12 - top). The layer's composition could not be determined. The layer was easily removed with a cotton cloth and iso-propanol which confirms that was formed due to contamination. After removing the layer, XRD measurement was repeated (Figure 3.12 - bottom). The XRD pattern show only BCC peaks and apart from peak intensities, no structural difference to the initial condition could be detected.

An additional XRD measurement was done with wobbling to increase the measured area. The measurement detected small peak splitting. As an example, the middle XRD pattern in Figure 3.12 presents partial scans in the range 50-60° 2θ, around the (200) reflection. From Sleiman and Huot [68] XRD measurements, the lattice parameter increases from 3.366 Å to 3.463 Å when the alloy contains about 1.2 wt.% of H (1.1 H/M). Since the XRD measurements in this study was done on a bulk sample, it was expected to find additional peaks at lower angles. As an example for the (200) plane, an additional peak would be observed within the range 53-54.6° 2θ. However, due to the width of the initial peak, an additional peak would be visible below 54°. This gives an estimation that structural changes can be detected only when the amount of H is above 0.3 H/M. Therefore, it is most likely that grains with slightly different lattice parameter contributed to the splitting of the peaks.

Based on Pourbaix diagram, hydride formation should be possible, provided low enough potential during chronoamperometric H charging. Preventing the occurrence of the predominant HER by decreasing cathodic overpotential might not be as problematic on H absorption as initially thought. There is some evidence that providing high enough overpotential can destabilize the oxide layer (lowering the energy barrier of the surface), which can lead to H absorption [5]. However, based on the relation between equilibrium pressure for H gas charging and potential for the electrochemical reaction at given T (from the equation 6 in [5]), the equilibrium potential equal to 100 bar is -1.09 V vs. $Ag/AgCl_{sat}$; applied potential in this work is below the equilibrium potential.

From the obtained results in this work and findings in published papers on electrochemical charging, the evidence for failed electrochemical H charging points towards oxide layer formed on the sample surface. The oxide layer can already form during polishing step [4]. In some of the research the surface was additionally treated with strong acid which effectively dissolves any oxide formed on the surface. However, in this work the samples were not treated with acid after polishing and ultrasonic cleaning thus it cannot be certain that the oxide layer was not already present before the charging. Further evidence on importance of sample

pre-treatment can be found in the Sleiman and Huot [68] study researching the dependence of H absorption ability of the TiVZrNbHf on particle size, pressure and temperature. At lower temperatures H absorption takes longer time to start after which full hydrogenation is reached relatively fast. This means, that the H requires sufficient amount of energy to overcome the surface barrier and move to the metal bulk. Relatively fast reaction kinetics after activation can be due to increased lattice distortion which lowers the surface energy barrier [31]. Based on the plot of the incubation period as a function of 1000/T by Sleiman and Huot [68], charging the HEA at RT is not possible without prior activation. After the alloy is activated, it starts to absorb H at RT within minutes [51]. Furthermore, Park et al. [54] investigated the effect of valence state of the surface on H absorption. Stable oxides have high valence state which effectively prevent H_2 gas dissociation. Destabilizing oxides to suboxides (lowering the valence state) can enable H absorption.

As evident from the experimental results and literature, without activation process (lowering surface valence state by oxide destabilization or dissolution) the absorption cannot occur at RT no matter the increased of the charging time or overpotential. Therefore, the state of the surface should be further investigated in relation to the surface pre-treatment before and after electrochemical charging.

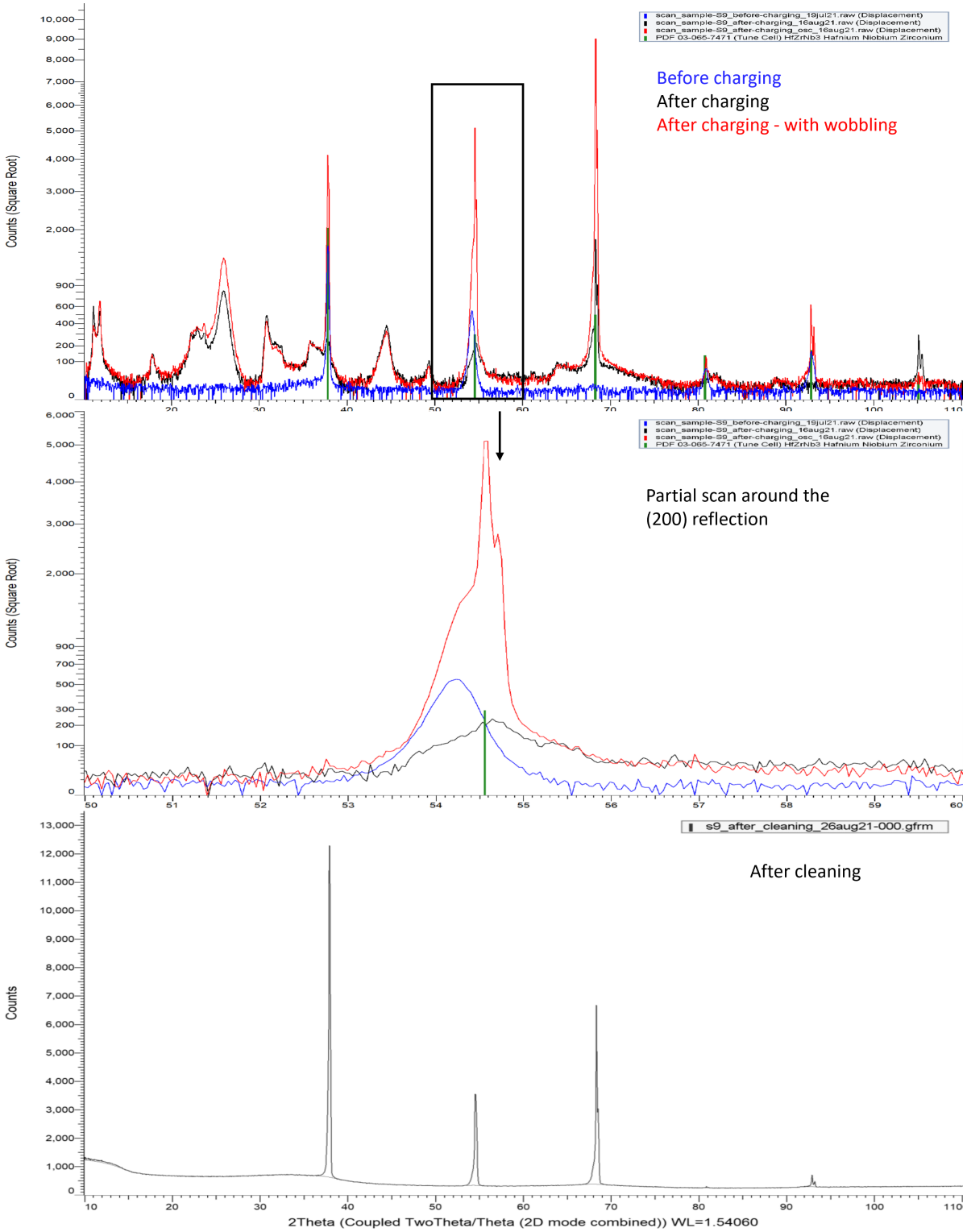

Figure 3.12: XRD patterns of the sample before (blue) and after H charging for 19 days (black) including results from wobbling (red); the middle XRD pattern shows close-up of the (200) split peak. The bottom figure shows XRD pattern for the charged sample after surface cleaning.

3.3. Molecular dynamics simulation results

3.3.1. TiVZrNbHf without hydrogen

The normalization of SQS used in this work is represented by how much the occurrence of each pair type found in the unrelaxed SQS lattice differs from the occurrence in the perfectly random structure. For an equiatomic solid solution with 5 atomic species there are 25 unique arrangements[1] for atoms to form pairs. Ideally, the same atom pairs would have a probability of 4 % while the unlike atom pairs have a probability of 8 %. In Table 3.3 shows values of normalization factor (f_{norm}) that is defined as a ratio between found occurrence in SQS and the occurrence for perfectly random structure.

The most frequently found 1st NN pair in the BCC and FCC SQS is Hf-Hf with the most deviation from the ideal value. In the FCC SQS the deviation between f_{norm} for pairs with different atom species is smaller than for the BCC. For the least frequent 1 NN pair in BCC is Hf-Nb and in FCC is Nb-Nb.

Table 3.3: Normalization factor (f_{norm}) for the 1st nearest neighboring (1 st NN) pairs for the BCC and FCC simulation cell.

1 NN pair	Ti-Ti	Zr-Zr	Hf-Hf	V-V	Nb-Nb	Ti-Zr	Ti-Hf	Ti-V	Ti-Nb	Zr-Hf	Zr-V	Zr-Nb	Hf-V	Hf-Nb	V-Nb
BCC	1	0.95	1.30	0.95	0.90	1.03	0.90	0.85	1.23	0.93	1.08	1.03	1.08	0.80	1.05
FCC	1	0.93	1.33	0.93	0.83	0.92	0.95	1.03	1.10	0.93	1.08	1.07	1	0.98	0.95

In the BCC cell the total number of O-sites is 375 and 750 for T-sites. Distinguishing of O- and T-sites in the relaxed BCC cell to obtain information on H occupational position has been proven difficult. The reason for that is that the octahedral position in unrelaxed BCC is really a saddle point in terms of distances to nearest atoms. Furthermore, in the relaxed BCC HEA positions of interstices are distorted. For the FCC SQS cell the total number of O-sites is 125 and 250 of T-sites.

Determination of O- and T-sites was much easier compared to BCC structure since there is a narrow window consisting of 3 metal atoms that clearly separates the T-sites from the O-sites.

Relaxed BCC and FCC cells without H have lattice parameters 3.354 Å and 4.244 Å, respectively. The relaxed cells are shown in Figure 3.13. The BCC lattice parameter is similar to the theoretical values of 3.36 and 3.40 obtained by Fazakas et al. [19] and Casillas-Trujillo et al. [9], respectively; experimental, the lattice constant has been reported in a range 3.365 - 3.385 Å. The theoretical values are expected to be smaller than the experimental since the system is computed at 0 K.

For FCC, the lattice parameter of hydrogenated TiVZrNbHf (2.09 wt. % H) of 4.582 Å was reported by Ek et al. [16]. The theoretical value of the lattice constant is even larger compared to the BCC since the relaxation of FCC was done without H and volume was fixed during MD calculation.

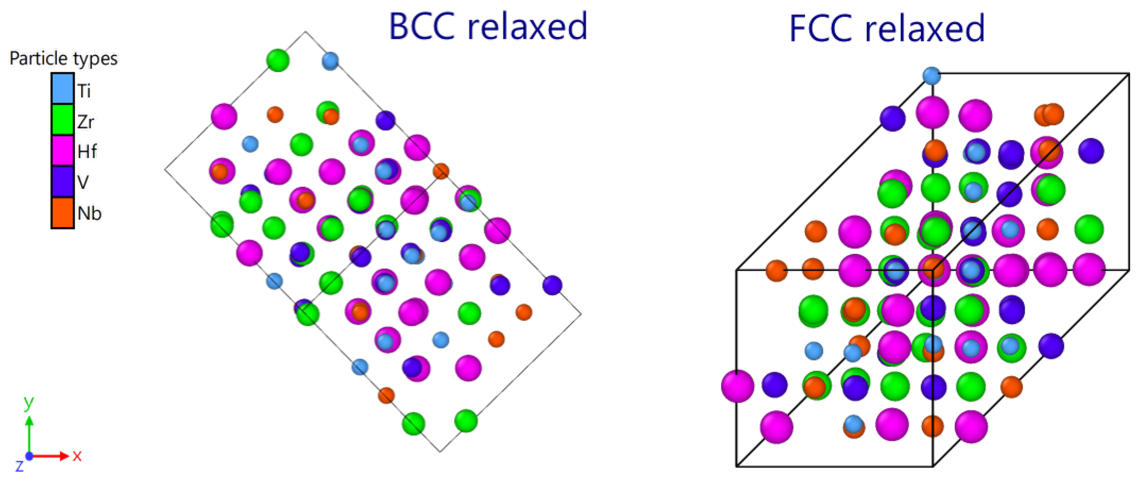

Figure 3.13: Simulation cell of the relaxed BCC (left) and FCC (right).

[1] A distinction between unlike atom pairs, such as XY and YX, is not possible

3.3.2. Stability of molecular dynamics runs

For determination of stability of each MD run, a time analyzed τ (see Table 2.4) for each defined system was divided into 4 parts to see whether the average total energies (E_{tot}) reached stationary state or not.

The obtained averages of E_{tot} show that all the defined systems for H_x in the BCC lattice reached stationary state (Figure 3.14). In the case of H_x in the FCC lattice stationary state was reached only for the systems with 300 H (Figure 3.14). The systems with 175 H and 250 H show a consistent decrease of E_{tot}. This results shows that the total time of the MD runs should be longer for the FCC systems with 175H and 250H.

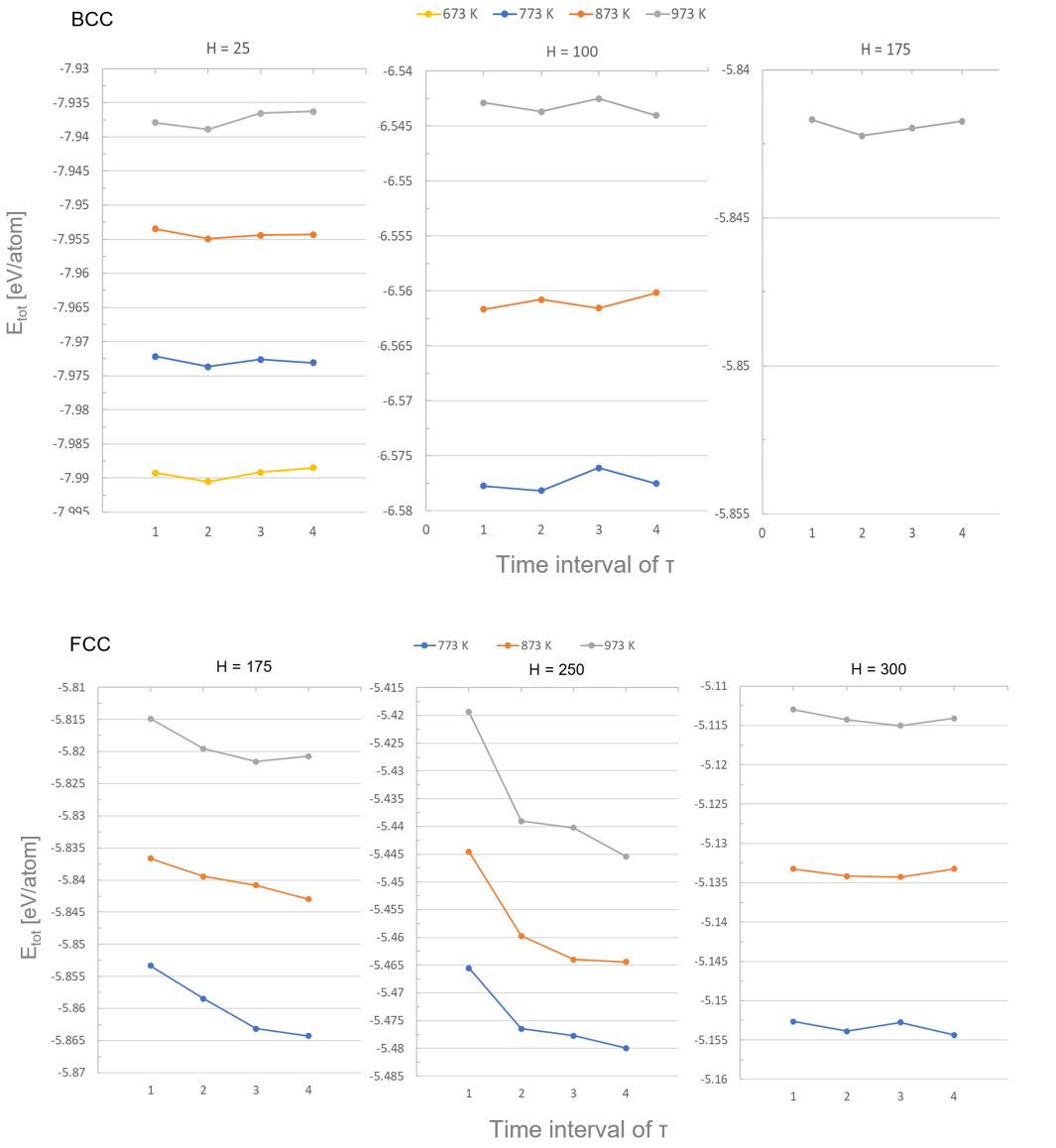

Figure 3.14: Average values of total energy (E_{tot}) in each quarter of analyzed run time - BCC (top) and FCC (bottom).

3.3.3. Hydrogen diffusivity and activation energy

For all MD simulations atoms were free to move. From the results of the mean square displacement (MSD) of the metal atoms (Figure 3.15) it is evident that the alloying atoms only oscillate around their initial position but do not diffuse. For H atoms all MSD plots show to be linear with time (Figure 3.16), meaning that H indeed diffuses.

From the observation of Arrhenius plots in Figure 3.17 almost all fitted lines (for H/M > 0.2) have a good linear regression fit ($R^2 > 0.95$). The D_H values are inversely proportional with the temperature change. Only the BCC with 25 H shows the highest deviation from the fit ($R^2 = 0.93$). This indicates that H diffusivity at

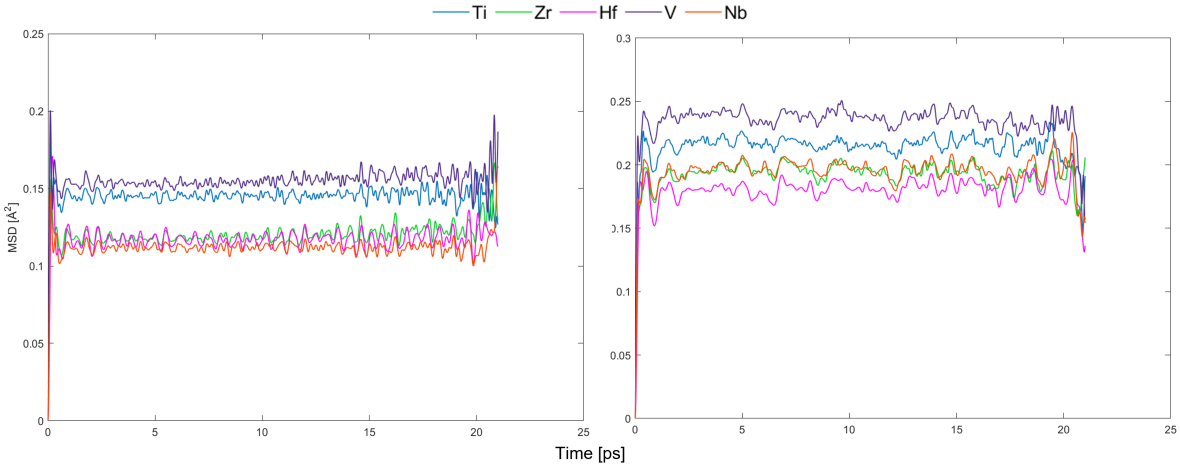

Figure 3.15: Mean square displacement (MSD) for metal atoms in TiZrHfVNb as a function of time; obtained from BCC (left) and FCC (right) MD simulation with 175 H at 973 K.

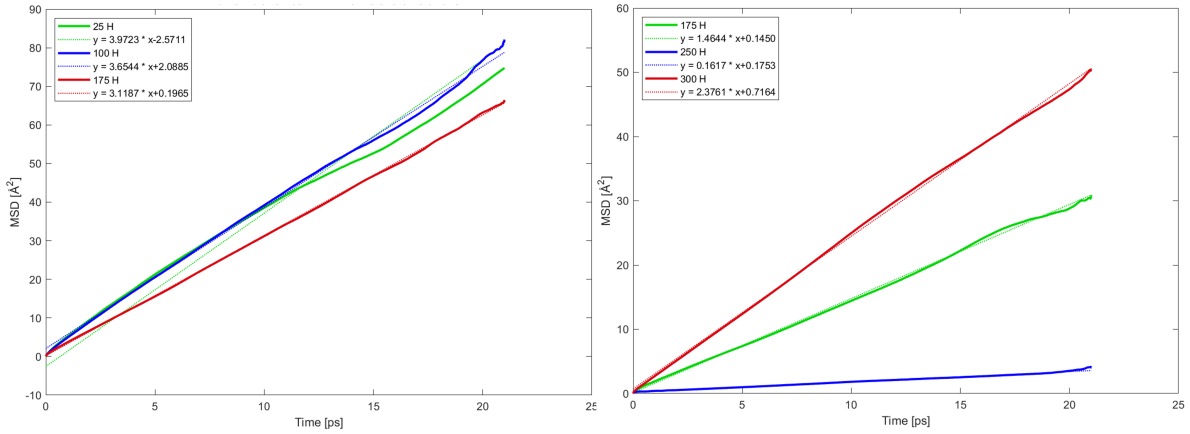

Figure 3.16: Mean square displacement (MSD) with linear regression fit for H atoms in TiZrHfVNb as a function of time; obtained from BCC (left) and FCC (right) MD simulation with different H concentrations at 973 K.

low H concentration (H/M = 0.2) might not be inversely proportional with the temperature change. However, such a relation should be further confirmed by acquiring more data points in this temperature range.

The values of E_a and D_0, estimated from Arrhenius equation 2.3, are presented in Table 3.4 and plotted in Figure 3.18 as a function of H/M. Noticeably, the values obtained for the systems that did not reach stable state (FCC with 175H and 250 H - Figure 3.14) show much grater uncertainty than the rest. The comparison between BCC with 0.8 H/M and FCC with 2.4 H/M shows the E_a and D_0 values to be about the same. However, it is reasonable to expect the values of E_a for BCC to be lower compare to the values for FCC since the BCC structure is less densely packed.

Dependency of D_H on H concentration can be observed by plotting D_H as a function of H/M (Figure 3.19). When comparing the D_H values of BCC and FCC at 1.4 H/M, the D_H in the BCC lattice is (two times) larger than the FCC, as expected. In BCC at 973 K, D_H decreases by ~22 % when the concentration increases from 0.2 to 1.4 H/M. At the same temperature, D_H in FCC first decreases until 2 H/M is reached. Further increase of the H concentration leads to a sharp rise in D_H with the highest value at 2.4 H/M (Figure 3.20). This shows that the H concentration has much grater effect on D_H in FCC compare to BCC.

An insight on the effect of H/M on D_H can be obtained in relation to E_a and D_0 as they are both intrinsic properties related to a structure and composition of an alloy. The value of E_a is related to the average height of the potential barriers that H needs to overcome for jumping into the next interstitial site. In the TiVZrNbHf a jump rate of H and energies of interstitial sites vary due to the effect of the configurational disorder (HEA core effect - see Subsection 1.1.1).

For D_0 the surrounding environment of H needs to be considered. For example, when H sits in an O-

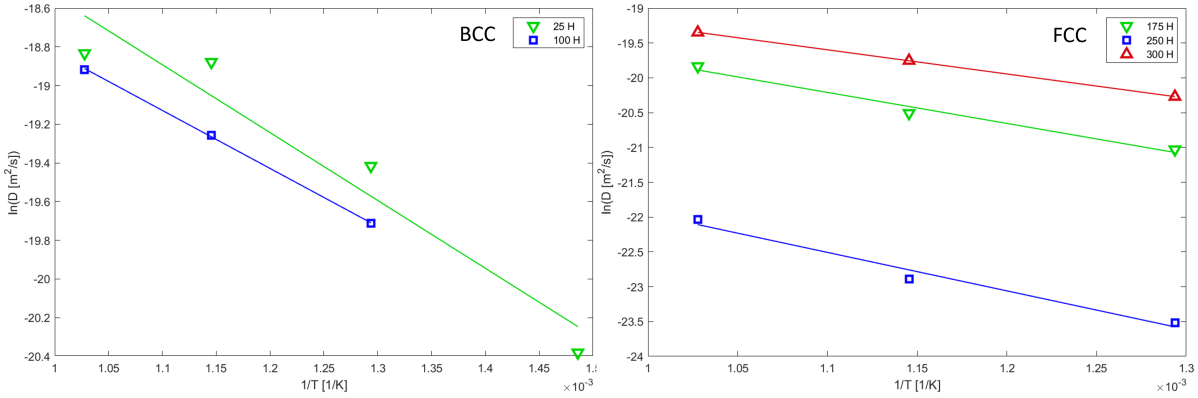

Figure 3.17: Arrhenius plot for BCC (left) and FCC (right) obtained from different H concentrations; for BCC with 25 H the diffusivity values show the most deviation from the fitted line, indicating a non-linear trend.

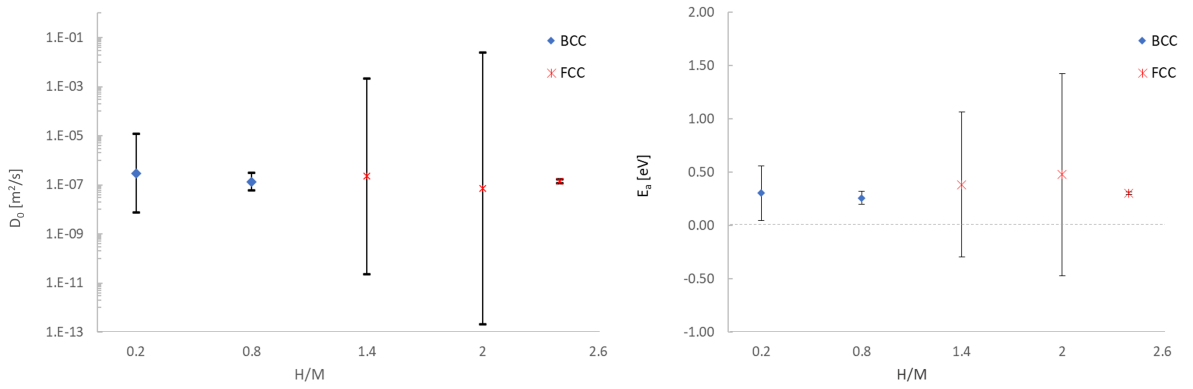

Figure 3.18: Values for D_0 (left) and E_a (right) are plotted as a function of H/M; the error bars show 95 % confidence interval.

site of FCC lattice with one type of matrix atom, H has an equal probability[2] to make a jump to either of the surrounding T-sites. In this case, the probability changes only if another H is occupying a neighboring site. However, in the HEA this probability is not equal and it is affected by the atomic environment.

In the case of BCC, at low H/M the most favorable interstitials are expected to be occupied first. These sites have lower energies (deeper energy well), meaning that the surrounding potential barriers are on average higher and it would require more energy for H to escape. At low H/M there is very small chance for H-H interaction and most of the neighboring sites are unoccupied, the probability of the H atom to make a jump depends mostly on the surrounding environment. Therefore, the limiting factor on D_H at low H/M would be the amount of provided energy. When H/M increases, there is a higher chance that the more energetically favorable sites (sites with the lowest energy) are already occupied. Therefore, some H atoms start to occupy less favorable sites where on average the surrounding barriers are lower which requires less energy for a H atom to make a jump. However, the probability of H-H interaction also increases which means that H movement does not depend only on the amount of provided energy anymore but also on the availability of the neighboring sites. Such reasoning indicates that by increasing H/M in BCC the average height of the potential barriers (E_a) and the probability for successful jump (D_0) decreases.

[2]Asssuming the initial lattice has no defects.

Table 3.4: Diffusivity (D_H), pre-exponential factor (D_0) and activation energy (E_a) for H in TiVZrNbHf obtained from the slope of MSD using Einstein relation; the data used for calculation of the values was taken from the last time interval τ (Table 2.4).

Structure	# H	T	D_H	D_0	E_a
		[K]	[m^2/s]		[eV]
BCC	25	673	1.4 E-09	2.95 E-07	0.30
		773	3.7 E-09		
		873	6.3 E-09		
		973	6.6 E-09		
	100	773	2.7 E-09	1.33 E-07	0.26
		873	4.3 E-09		
		973	6.1 E-09		
FCC	175	773	7.4 E-10	2.24 E-07	0.38
		873	1.2 E-09		
		973	2.4 E-09		
	250	773	6.1 E-11	7.29 E-08	0.48
		873	1.1 E-10		
		973	2.7 E-10		
	300	773	1.6 E-09	1.40 E-07	0.30
		873	2.6 E-09		
		973	4.0 E-09		

The D_H values for FCC show peculiar trend (Figure 3.20): the value of D_H is higher by a factor of 1.6 for the case of the highest H concentration (2.4 H/M) in comparison to the lowest concentration (1.4 H/M). Some clues about D_H in FCC could be found from the published studies on TiVZrNbHf. Nygård et al. [48] and Karlsson et al. [31] found that, H has more preference to occupy T-sites[3] in FCC and that at ~2 H/M some of the T-sites are not occupied. In the FCC simulation supercell of this work there are 250 T-sites which theoretically, at 2 H/M all of the T-sites are occupied by H. By assuming that H inside FCC lattice indeed spends more time inside T-sites and from the D_H that was found to be the slowest at 2 H/M, it seems that H is mostly trapped in T-sites and only occasionally makes a jump from T- to T-site through O-site.

In general, H atoms inside a metal experience a repulsive force between each other and based on the Switendick criterion [72] prefer to be no closer than 2.1 Å to another H atom. This indicates that the optimum hydrogen distribution where the repulsive interaction between H atoms is the lowest, can be achieved when H atoms are positioned inside T-sites. Therefore, a H atom would need to overcome the energy barrier as well as the additional repulsive force from the surrounding H atoms occupying the neighboring T-sites to jump. This would explain the lowest values of D_H at 2 H/M in FCC obtained from the MD simulations in this work (Figure 3.20). Even the temperature increase have a little contribution to the D_H increase (Figure 3.19). Once H concentration exceeds 2 H/M the only available sites left for H to occupy are O-sites. Since most of the O-sites are now surrounded by already occupied T-sites it is expected for the H atoms inside O-sites to have an effect on the behavior of the surrounding H atoms. From the steep rise of D_H when H/M > 2 (Figure 3.20) it is possible that an additional H inside O-site affects energies of the surrounding T-sites enough to increasing their energies due to repulsive force of H-H. Therefore, this would make much easier for the H atoms in the neighboring T-sites to make a jump.

[3] In general, H prefers to occupy larger O-sites than smaller T-sites in FCC structure. Thus far, it is not clear the relation of H preferential occupation with site volume in HEAs.

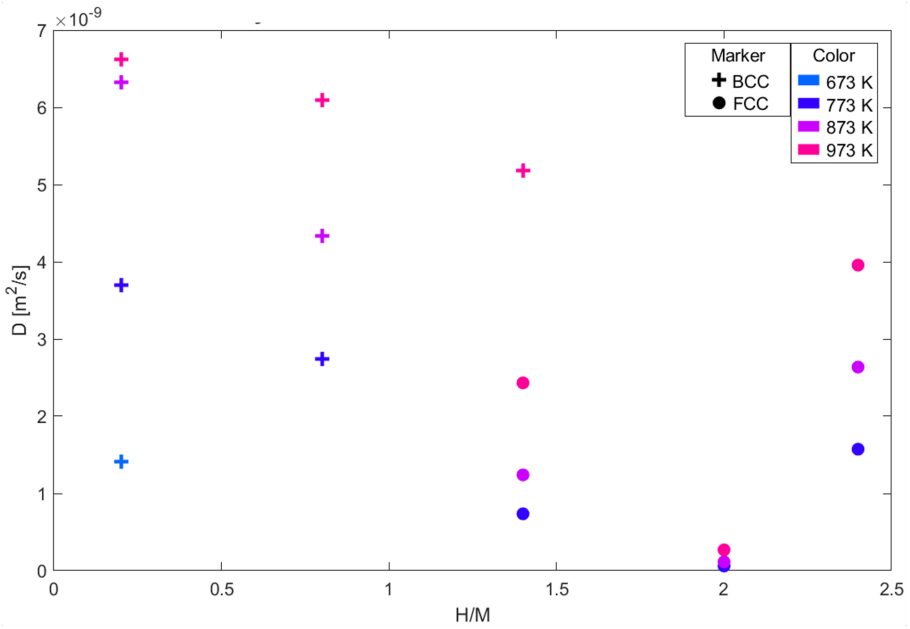

Figure 3.19: Diffusivity values as a function of H/M for BCC and FCC at different temperature.

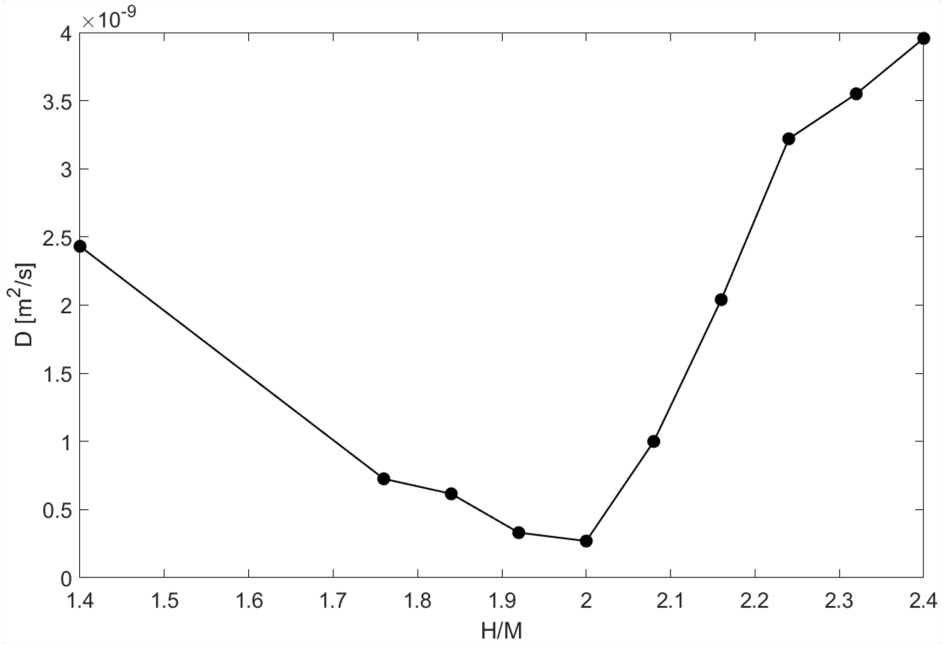

Figure 3.20: Diffusivity values for H in FCC plotted against H/M.

3.3.4. Hydrogen preferential site occupation

To gain more insight and support of the predictions made based on D_H in relation to H/M, a time and preferred environment of H occupancy were further analyzed in FCC[4]. First, a rough determination of a jump was based on finding a time step at which the observed H atom leaves the volume of a site. A site volume was determined for when metal atoms form tetrahedron or octahedron for T- or O-sites, respectively. The accuracy of the Matlab code to correctly detect an actual jump was inspected visually. It was noticed that H very often makes an attempt to jump that is registered as a jump. Therefor, to reduced detection of the attempts as jumps, an additional condition was used; for when H is found outside a site volume, a distance traveled was then measured perpendicular to the plane from where H left the site. If H covered a distance greater than 0.4 Å it was considered a jump. The decision on the distance limit is based on 1/24 of the FCC body diagonal which would be on average 1/2 of a distance between a site's plane and a center of a new site. Due to the lattice distortion few attempts were still detected as jumps but the criterion on average properly detected movement from one interstitial position to another.

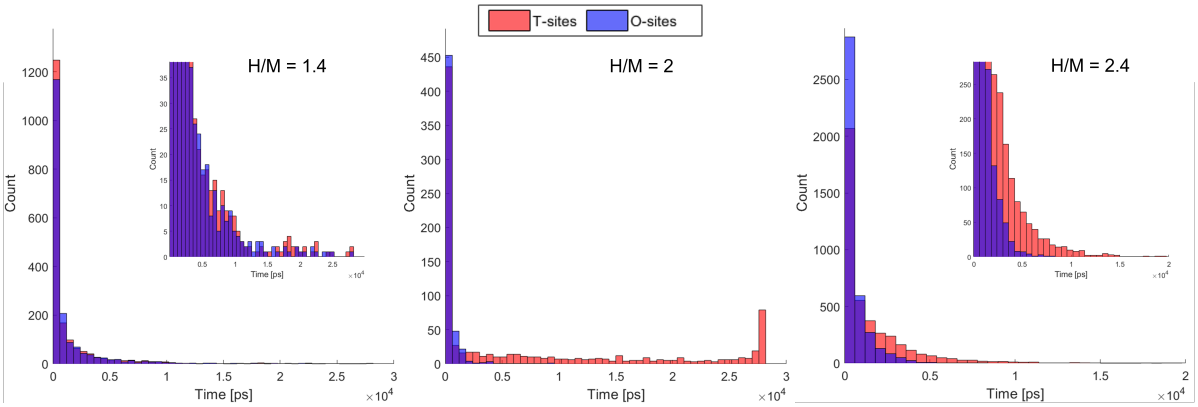

Figure 3.21: Histograms for H occupation times inside T- and O-sites before a jump for FCC at 873 K; for 1.4 and 2.4 H/M have an additional enlarged area to show counts for longer times.

The analysis of obtained H occupation times resulted for the majority of H to reside for about 0.45 ps inside an interstitial before jumping to the next one (Figure 3.21). As observed already in trends of diffusivity, H stays inside T-site much longer when H/M = 2 than at lower or higher H/M. From the histograms for 1.4 there is barely visible difference between occupation times inside T- and O-sites (enlarged area in Figure 3.21), with slightly longer times for H inside T-sites. This becomes more clear for 2.4 H/M where H occupies T-site for longer times compared to O-sites. It also shows that H atoms are no longer trapped inside T-sites as for H/M = 2, possibly due to disturbance from additional H atoms placed inside O-sites.

To obtain better contrast between H time inside O- and T-sites additional processing of H occupation times was done. To filter out the shorter times, an average time and the maximum time of each H atom inside T- and O-sites was obtained. The average time inside each interstitial type is determined as a sum of all times inside T- or O-sites divided by the number of times H was found in T- or O-sites; for the maximum time was simply to find the longest time that H spends inside an O- and in a T-site. Figure 3.22 shows the time averages and the maximum times of individual H atoms in T- and O-sites for FCC at 873 K. At 1.4 H/M the distribution of O- and T-sites occupational times are overlapping. There is a slight preference of H towards T-sites; 52 % of the total time H spends inside T-sites and on average 1.03 ps in T-sites before it jumps to the next site while an average time of H in O-sites is 0.98 ps. The results for FCC at 1.4 H/M show that only about 10 % of H is trapped in T-sites where the jump pathway T-O-T is available and O-sites seem to be energetically as favorable as T-sites.

As predicted before, H at 2 H/M has much stronger preference to occupy T-sites. With increasing H concentration (up to 2 H/M), H spends on average less time (0.5 ps) inside O-sites which indicates that jumping to another T-site through O-site becomes much more difficult. The results of maximum occupation times show that 36 % of H atoms are completely trapped (98 % of the total time) inside T-sites. When accounted also H atoms that spend more than 70% of the total time inside T-sites, this results in 78 % of H being trapped inside T-sites. Comparing the results between 1.4 and 2 H/M shows that with increasing H/M jump pathway T-O-T becomes much more difficult.

[4] In BCC it has been proven difficult to distinguish when H is inside O- or T-sites, as explained in Subsection 3.3.1.

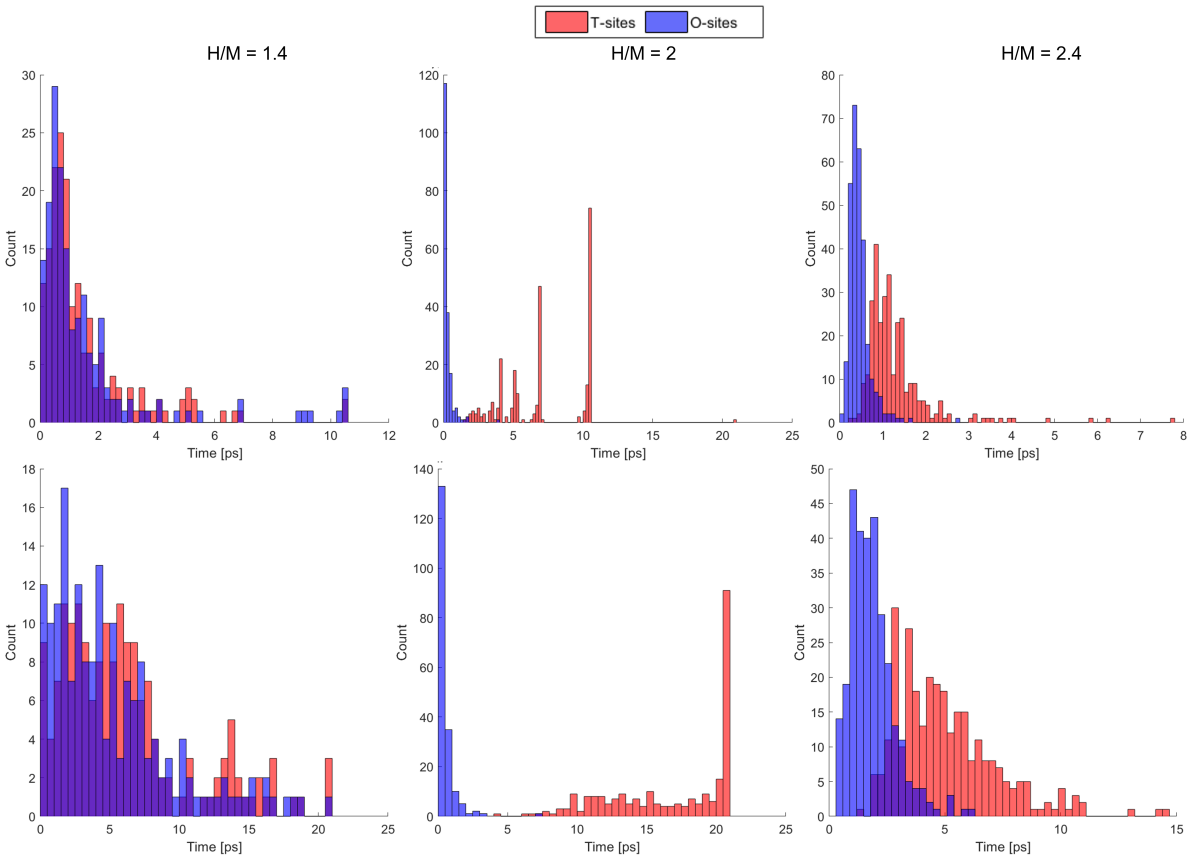

Figure 3.22: Occupation times for each individual H atom; the first column dt(avr) shows average time that a H atom occupies a site and the second column shows average time of a H atom occupying T- and O-sites; last column dt(max) is maximum time found for a H atom to occupy T- and O-site. The times were obtained for FCC at 873 K.

At 2.4 H/M the distribution of H average and maximum occupation times inside T-sites shifts towards shorter times (Figure 3.22). Compared to 1.4 H/M, the distribution at 2.4 H/M has clearer distributions for O- and T-sites. The results in Figure 3.22 show that H at 2.4 H/M is neither blocked in O-sited nor extremely mobile but it is still much more mobile in comparison to 1.4 H/M; H atoms spend in O-sites almost three times less time than at 1.4 H/M. The average/maximum occupation time of H in O- and T-site was found to be 0.42/1.87 ps and 1.11/5.04 ps, respectively. As mentioned before, a possible explanation of those results would be that increased number of neighboring H atoms surrounding each other causes a strong repulsion and/or asymmetry of occupied sites within the lattice unit cell (20 % of interstitials are unoccupied). In this case, H preference to occupy certain site depends mostly on a local density of H atoms.

The examination of the H preferential site occupation in FCC results in similar occupancy of both T- and O-sites at lower H/M while occupation of T-sites is preferred with increasing H/M. However, at 2 H/M not all T-sites are fully occupied. The results obtain in this study are similar to the experimental observations of H occupancy by Karlsson et al. [31] where H was found to occupy both T- and O-sites at low H/M (in-situ at 500 °C, 50 bar D_2) while at H/M ~ 2 (ex-situ at room temperature) about 93 % of T-site were occupied. Another study done by Nygård et al. [48] also found that H at 2 H/M occupies the majority of T-sites and tends to avoid T-sites with smaller volume, which leads to a small occupation of O-sites.

4

Conclusions

In this work the main objective was to investigate hydrogen diffusivity in relation to hydrogen absorption kinetics in equimolar TiVZrNbHf high entropy alloy. The results lead to the following conclusions:

1. The experimental approach to hydrogenate the alloy by the electrochemical charging method did not result in hydrogen absorption. During charging the alloy without prior CV scan for longer times, the HER occurred and no structural changes due to absorbed H could be detected. This indicates that the alloy's surface was already passivated. The presence of an oxide layer is know to severely limit the absorption of hydrogen into the bulk.

2. The simulation results are as follows:

   - D_H shows linear relation to the temperature in both BCC and FCC at higher H concentrations (H/M > 0.2); increase in temperature leads to linear increase in D_H. At lower H concentration the D_H shows non-linear trend with temperature.
   - In BCC lattice D_H is higher compare to FCC.
   - The values of activation energy and pre-exponential factor were estimated to be in the range of 0.26 – 0.48 eV and 0.73 – 2.95 $\times 10^{-7} m^2/s$, respectively.

3. Based on MD simulations, the change in hydrogen diffusivity with respect to the H/M shows to be different for each crystal structure:

   - In BCC the increase of H concentration causes slight decrease in D_H.
   - In FCC, the D_H was found to be the highest at 2.4 H/M while at 2 H/M the D_H was the lowest.

4. Examination of D_H, activation energy and pre-exponential factor at different H/M indicates that H-H interaction influences the D_H. With increasing H/M it is possible that the repulsive force from H-H interaction increases the energy barrier and thus limits the H movement.

5. The analysis of H occupation sites found that:

   - At lower H/M in FCC the H occupation time is similar for both O- and T-sites while H preference changes towards longer occupation times of T-sites when H/M increases.
   - At 2 H/M in FCC most of the H atoms are trapped inside T-sites, possibly as a result of the repulsive interaction between H atoms is the lowest.

5

Recommendations

1. The electrochemical process of H absorption in TiVZrNbHf high entropy alloy should be further investigated in relation to the state of the surface:

   - Characterization of the surface before and after charging (e.g. by X-ray photoelectron spectroscopy (XPS)) for better understanding of surface conditions.
   - The effect of the surface pre-treatment (e.g. rougher surface, etching the surface) on the H absorption rate.

   Additionally, further testing of the charging parameters known to affect H absorption is needed:

   - The effect of pH solution on the rate of H absorption
   - Using a recombination poison to prevent H_2 formation or use of a catalyst (e.g. a thin Pd layer) for easier H dissociation

2. From the simulation analysis in this work the following observations should be further investigated:

   - The relationship of H diffusivity with temperature at low H concentration in BCC should be determined more accurately by acquiring more values of the H diffusivity at several temperatures within 773 - 973 K range.
   - Further optimization of M-H and H-H potential in the HEA is needed for more accurate determination of activation energy and pre-exponential factor as well as for the determination of the amount of repulsive force between H atoms in FCC.

Bibliography

[1] DOE Technical Targets for Onboard Hydrogen Storage for Light-Duty Vehicles. https://www.energy.gov/eere/fuelcells/doe-technical-targets-onboard-hydrogen-storage-light-duty-vehicles.

[2] Y. A. Alshataif, S. Sivasankaran, F. A. Al-Mufadi, A. S. Alaboodi, and H. R. Ammar. Manufacturing Methods, Microstructural and Mechanical Properties Evolutions of High-Entropy Alloys: A Review. Metals and Materials International, 26(8):1099–1133, Aug 2020. ISSN 2005-4149. doi: 10.1007/s12540-019-00565-z. URL https://doi.org/10.1007/s12540-019-00565-z.

[3] N. Altman and M. Krzywinski. Simple linear regression. Nature Methods, 12(11):999–1000, Nov 2015. ISSN 1548-7105. doi: 10.1038/nmeth.3627. URL https://doi.org/10.1038/nmeth.3627.

[4] C. Z. Antoine and S. Berry. H in Niobium: Origin And Method Of Detection. AIP Conference Proceedings, 671(1):176–189, 2003. doi: 10.1063/1.1597367. URL https://aip.scitation.org/doi/abs/10.1063/1.1597367.

[5] A. M. Bedoch, G. Y. Koga, R. P. Nogueira, and G. Zepon. On the electrochemical hydrogenation of Nb: An insight into the effect of hydrogen absorption on the kinetics of the hydrogen evolution reaction. Electrochimica Acta, 389:138626, Sep 2021. ISSN 0013-4686. URL https://www.sciencedirect.com/science/article/pii/S0013468621009166.

[6] K. Biswas, J.-W. Yeh, P. P. Bhattacharjee, and J. T. DeHosson. High entropy alloys: Key issues under passionate debate. Scripta Materialia, 188:54–58, Nov 2020. ISSN 1359-6462. URL https://www.sciencedirect.com/science/article/pii/S1359646220304590.

[7] N. D. d. Campos, F. S. Pereira, and M. F. d. Oliveira. Analysis of Processing Parameters to Avoid Additional Oxygen Contamination During Production of Zr-based Bulk Metallic Glasses by Suction Casting in an Arc-melting Furnace. Materials Research, 24, 2021. doi: 10.1590/1980-5373-MR-2020-0276. URL https://doi.org/10.1590/1980-5373-MR-2020-0276.

[8] B. Cantor, I. T. H. Chang, P. Knight, and A. J. B. Vincent. Microstructural development in equiatomic multicomponent alloys. Materials Science and Engineering: A, 375-377:213–218, Jul 2004. ISSN 0921-5093. URL https://www.sciencedirect.com/science/article/pii/S0921509303009936.

[9] L. Casillas-Trujillo, U. Jansson, M. Sahlberg, G. Ek, M. M. Nygård, M. H. Sørby, B. C. Hauback, I. A. Abrikosov, and B. Alling. Interstitial carbon in bcc HfNbTiVZr high-entropy alloy from first principles. Phys. Rev. Materials, 4:123601, Dec 2020. doi: 10.1103/PhysRevMaterials.4.123601. URL https://link.aps.org/doi/10.1103/PhysRevMaterials.4.123601.

[10] S.-K. Chen, P.-H. Lee, H. Lee, and H.-T. Su. Hydrogen storage of C14-CruFevMnwTixVyZrz alloys. Materials Chemistry and Physics, 210:336–347, May 2018. ISSN 0254-0584. URL https://www.sciencedirect.com/science/article/pii/S0254058417306247.

[11] H.-J. Christ, M. Decker, and S. Zeitler. Hydrogen diffusion coefficients in the titanium alloys IMI 834, Ti 10-2-3, Ti 21 S, and alloy C. Metallurgical and Materials Transactions A, 31(6):1507–1517, Jun 2000. ISSN 1543-1940. doi: 10.1007/s11661-000-0161-8. URL https://doi.org/10.1007/s11661-000-0161-8.

[12] J. Dąbrowa, M. Zajusz, W. Kucza, G. Cieślak, K. Berent, T. Czeppe, T. Kulik, and M. Danielewski. Demystifying the sluggish diffusion effect in high entropy alloys. Journal of Alloys and Compounds, 783:193–207, Apr 2019. ISSN 0925-8388. URL https://www.sciencedirect.com/science/article/pii/S0925838818348576.

[13] J. Dąbrowa and M. Danielewski. State-of-the-Art Diffusion Studies in the High Entropy Alloys. Metals, 10(3), 2020. ISSN 2075-4701. doi: 10.3390/met10030347. URL https://www.mdpi.com/2075-4701/10/3/347.

[14] S. V. Divinski, A. V. Pokoev, N. Esakkiraja, and A. Paul. A Mystery of "Sluggish Diffusion" in High-Entropy Alloys: The Truth or a Myth? Diffusion Foundations, 17:69–104, 2018. ISSN 2296-3642. doi: 10.4028/www.scientific.net/DF.17.69. URL https://www.scientific.net/DF.17.69.

[15] P. Edalati, R. Floriano, A. Mohammadi, Y. Li, G. Zepon, H.-W. Li, and K. Edalati. Reversible room temperature hydrogen storage in high-entropy alloy TiZrCrMnFeNi. Scripta Materialia, 178:387–390, Mar 2020. ISSN 1359-6462. URL https://www.sciencedirect.com/science/article/pii/S1359646219307286.

[16] G. Ek, Ø. S. Fjellvåg, P. Vajeeston, J. Armstrong, M. Sahlberg, and U. Häussermann. Vibrational properties of High Entropy Alloy based metal hydrides probed by inelastic neutron scattering. Journal of Alloys and Compounds, 877:160320, Oct 2021. ISSN 0925-8388. URL https://www.sciencedirect.com/science/article/pii/S0925838821017291.

[17] G. Ek, M. M. Nygård, A. F. Pavan, J. Montero, P. F. Henry, M. H. Sørby, M. Witman, V. Stavila, C. Zlotea, B. C. Hauback, and M. Sahlberg. Elucidating the Effects of the Composition on Hydrogen Sorption in TiVZrNbHf-Based High-Entropy Alloys. Inorganic Chemistry, 60(2):1124–1132, Jan 2021. ISSN 0020-1669. doi: 10.1021/acs.inorgchem.0c03270. URL https://doi.org/10.1021/acs.inorgchem.0c03270.

[18] S. Fashu, M. Lototskyy, M. W. Davids, L. Pickering, V. Linkov, S. Tai, T. Renheng, X. Fangming, P. V. Fursikov, and B. P. Tarasov. A review on crucibles for induction melting of titanium alloys. Materials & Design, 186:108295, Jan 2020. ISSN 0264-1275. URL https://www.sciencedirect.com/science/article/pii/S0264127519307336.

[19] É. Fazakas, V. Zadorozhnyy, L. K. Varga, A. Inoue, D. V. Louzguine-Luzgin, F. Tian, and L. Vitos. Experimental and theoretical study of Ti20Zr20Hf20Nb20X20 (X=V or Cr) refractory high-entropy alloys. International Journal of Refractory Metals and Hard Materials, 47:131–138, Nov 2014. ISSN 0263-4368. URL https://www.sciencedirect.com/science/article/pii/S0263436814001516.

[20] M. Feuerbacher, T. Lienig, and C. Thomas. A single-phase bcc high-entropy alloy in the refractory Zr-Nb-Ti-V-Hf system. Scripta Materialia, 152:40–43, Jul 2018. ISSN 1359-6462. URL https://www.sciencedirect.com/science/article/pii/S1359646218302227.

[21] R. Floriano, G. Zepon, K. Edalati, G. L. Fontana, A. Mohammadi, Z. Ma, H.-W. Li, and R. J. Contieri. Hydrogen storage in TiZrNbFeNi high entropy alloys, designed by thermodynamic calculations. International Journal of Hydrogen Energy, 45(58):33759–33770, Nov 2020. ISSN 0360-3199. URL https://www.sciencedirect.com/science/article/pii/S0360319920334649.

[22] R. Floriano, G. Zepon, K. Edalati, G. L. Fontana, A. Mohammadi, Z. Ma, H.-W. Li, and R. J. Contieri. Hydrogen storage properties of new A3B2-type TiZrNbCrFe high-entropy alloy. International Journal of Hydrogen Energy, 46(46):23757–23766, Jul 2021. ISSN 0360-3199. URL https://www.sciencedirect.com/science/article/pii/S0360319921016281.

[23] M. C. Gao, D. B. Miracle, D. Maurice, X. Yan, Y. Zhang, and J. A. Hawk. High-entropy functional materials. Journal of Materials Research, 33(19):3138–3155, 2018. ISSN 0884-2914. doi: 10.1557/jmr.2018.323. URL https://www.cambridge.org/core/article/highentropy-functional-materials/1A80E6D3AC626FC4EC51944FFAABD22E.

[24] E. P. George, D. Raabe, and R. O. Ritchie. High-entropy alloys. Nature Reviews Materials, 4(8):515–534, Aug 2019. ISSN 2058-8437. doi: 10.1038/s41578-019-0121-4. URL https://doi.org/10.1038/s41578-019-0121-4.

[25] I. A. Hassan, H. S. Ramadan, M. A. Saleh, and D. Hissel. Hydrogen storage technologies for stationary and mobile applications: Review, analysis and perspectives. Renewable and Sustainable Energy Reviews, 149:111311, Oct 2021. ISSN 1364-0321. URL https://www.sciencedirect.com/science/article/pii/S1364032121005980.

[26] Q. He and Y. Yang. On Lattice Distortion in High Entropy Alloys. Frontiers in Materials, 5:42, 2018. ISSN 2296-8016. doi: 10.3389/fmats.2018.00042. URL https://www.frontiersin.org/article/10.3389/fmats.2018.00042.

[27] M. Hirscher, V. A. Yartys, M. Baricco, J. Bellosta von Colbe, D. Blanchard, R. C. Bowman, D. P. Broom, C. E. Buckley, F. Chang, P. Chen, Y. W. Cho, J.-C. Crivello, F. Cuevas, W. I. David, P. E. de Jongh, R. V. Denys, M. Dornheim, M. Felderhoff, Y. Filinchuk, G. E. Froudakis, D. M. Grant, E. M. Gray, B. C. Hauback, T. He, T. D. Humphries, T. R. Jensen, S. Kim, Y. Kojima, M. Latroche, H.-W. Li, M. V. Lototskyy, J. W. Makepeace, K. T. Møller, L. Naheed, P. Ngene, D. Noréus, M. M. Nygård, S.-i. Orimo, M. Paskevicius, L. Pasquini, D. B. Ravnsbæk, M. Veronica Sofianos, T. J. Udovic, T. Vegge, G. S. Walker, C. J. Webb, C. Weidenthaler, and C. Zlotea. Materials for hydrogen-based energy storage – past, recent progress and future outlook. Journal of Alloys and Compounds, 827:153548, Jun 2020. ISSN 0925-8388. URL https://www.sciencedirect.com/science/article/pii/S0925838819347942.

[28] Y. Jien-Wei. Recent progress in high entropy alloys. Ann. Chim. Sci. Mat, 31(6):633–648, 2006.

[29] R. Johansson, R. Ahuja, O. Eriksson, B. Hjörvarsson, and R. H. Scheicher. Effect of uniaxial strain on the site occupancy of hydrogen in vanadium from density-functional calculations. Scientific Reports, 5(1):10301, May 2015. ISSN 2045-2322. doi: 10.1038/srep10301. URL https://doi.org/10.1038/srep10301.

[30] Y.-F. Kao, S.-K. Chen, J.-H. Sheu, J.-T. Lin, W.-E. Lin, J.-W. Yeh, S.-J. Lin, T.-H. Liou, and C.-W. Wang. Hydrogen storage properties of multi-principal-component CoFeMnTixVyZrz alloys. International Journal of Hydrogen Energy, 35(17):9046–9059, Sep 2010. ISSN 0360-3199. URL https://www.sciencedirect.com/science/article/pii/S0360319910011882.

[31] D. Karlsson, G. Ek, J. Cedervall, C. Zlotea, K. T. Møller, T. C. Hansen, J. Bednarčík, M. Paskevicius, M. H. Sørby, T. R. Jensen, U. Jansson, and M. Sahlberg. Structure and Hydrogenation Properties of a HfNbTiVZr High-Entropy Alloy. Inorganic Chemistry, 57(4):2103–2110, Feb 2018. ISSN 0020-1669. doi: 10.1021/acs.inorgchem.7b03004. URL https://doi.org/10.1021/acs.inorgchem.7b03004.

[32] L. E. Klebanoff and J. O. Keller. 5 Years of hydrogen storage research in the U.S. DOE Metal Hydride Center of Excellence (MHCoE). International Journal of Hydrogen Energy, 38(11):4533–4576, Apr 2013. ISSN 0360-3199. URL https://www.sciencedirect.com/science/article/pii/S0360319913001365.

[33] L. Klebanoff. Chapter 3 - Historical Perspectives on Hydrogen, Its Storage, and Its Applications. CRC Press, 2012. doi: https://doi.org/10.1016/j.rser.2021.111311.

[34] I. Kunce, M. Polanski, and J. Bystrzycki. Structure and hydrogen storage properties of a high entropy ZrTiVCrFeNi alloy synthesized using Laser Engineered Net Shaping (LENS). International Journal of Hydrogen Energy, 38(27):12180–12189, Sep 2013. ISSN 0360-3199. URL https://www.sciencedirect.com/science/article/pii/S0360319913012676.

[35] I. Kunce, M. Polanski, and J. Bystrzycki. Microstructure and hydrogen storage properties of a TiZrNbMoV high entropy alloy synthesized using Laser Engineered Net Shaping (LENS). International Journal of Hydrogen Energy, 39(18):9904–9910, Jun 2014. ISSN 0360-3199. URL https://www.sciencedirect.com/science/article/pii/S0360319914004273.

[36] J. Liu, J. Xu, S. Sleiman, X. Chen, S. Zhu, H. Cheng, and J. Huot. Microstructure and hydrogen storage properties of Ti–V–Cr based BCC-type high entropy alloys. International Journal of Hydrogen Energy, 46(56):28709–28718, Aug 2021. ISSN 0360-3199. URL https://www.sciencedirect.com/science/article/pii/S0360319921023648.

[37] Y. Ma, Y. Ma, Q. Wang, S. Schweidler, M. Botros, T. Fu, H. Hahn, T. Brezesinski, and B. Breitung. High-entropy energy materials: challenges and new opportunities. Energy Environ. Sci., 14:2883–2905, 2021. doi: 10.1039/D1EE00505G. URL http://dx.doi.org/10.1039/D1EE00505G.

[38] A. Mehta and Y. H. Sohn. Fundamental Core Effects in Transition Metal High-Entropy Alloys: “High-Entropy” and “Sluggish Diffusion” Effects. Diffusion Foundations, 29:75–93, 5 2021. doi: 10.4028/www.scientific.net/DF.29.75.

[39] D. B. Miracle and O. N. Senkov. A critical review of high entropy alloys and related concepts. Acta Materialia, 122:448–511, Jan 2017. ISSN 1359-6454. URL https://www.sciencedirect.com/science/article/pii/S1359645416306759.

[40] M. K. Mohsun. Hydrogen Diffusion Influence on the Stabilizing Phases Behavior in the Ti-6Al-4V Alloy. In Advanced Materials and Engineering Materials X, volume 904 of Key Engineering Materials, pages 103–110. Trans Tech Publications Ltd, 12 2021. doi: 10.4028/www.scientific.net/KEM.904.103.

[41] K. T. Møller, T. R. Jensen, E. Akiba, and H.-w. Li. Hydrogen - A sustainable energy carrier. Progress in Natural Science: Materials International, 27(1):34–40, Feb 2017. ISSN 1002-0071. URL https://www.sciencedirect.com/science/article/pii/S1002007116303240.

[42] J. Montero, C. Zlotea, G. Ek, J.-C. Crivello, L. Laversenne, and M. Sahlberg. TiVZrNb Multi-Principal-Element Alloy: Synthesis Optimization, Structural, and Hydrogen Sorption Properties, 2019. ISSN 1420-3049. URL https://doi.org/10.3390/molecules24152799.

[43] J. Montero, G. Ek, L. Laversenne, V. Nassif, G. Zepon, M. Sahlberg, and C. Zlotea. Hydrogen storage properties of the refractory Ti–V–Zr–Nb–Ta multi-principal element alloy. Journal of Alloys and Compounds, 835:155376, Sep 2020. ISSN 0925-8388. URL https://www.sciencedirect.com/science/article/pii/S0925838820317394.

[44] J. Montero, G. Ek, L. Laversenne, V. Nassif, M. Sahlberg, and C. Zlotea. How 10 at% Al Addition in the Ti-V-Zr-Nb High-Entropy Alloy Changes Hydrogen Sorption Properties, 2021. ISSN 1420-3049. URL https://doi.org/10.3390/molecules26092470.

[45] J. Montero, G. Ek, M. Sahlberg, and C. Zlotea. Improving the hydrogen cycling properties by Mg addition in Ti-V-Zr-Nb refractory high entropy alloy. Scripta Materialia, 194:113699, Mar 2021. ISSN 1359-6462. URL https://www.sciencedirect.com/science/article/pii/S1359646220308216.

[46] S. Moon, C. Jeong, E. Byon, and Y. Jeong. Electrochemical Behavior of Titanium in NaOH Solutions. ECS Transactions, 1(4):151–156, jul 2006. doi: 10.1149/1.2215498. URL https://doi.org/10.1149/1.2215498.

[47] B. S. Murty, J. W. Yeh, and S. Ranganathan. Chapter 5 - Synthesis and Processing, pages 77–89. Butterworth-Heinemann, Boston, Jan 2014. ISBN 978-0-12-800251-3. URL https://www.sciencedirect.com/science/article/pii/B9780128002513000055.

[48] M. M. Nygård, W. A. Sławiński, G. Ek, M. H. Sørby, M. Sahlberg, D. A. Keen, and B. C. Hauback. Local order in high-entropy alloys and associated deuterides – a total scattering and Reverse Monte Carlo study. Acta Materialia, 199:504–513, Oct 2020. ISSN 1359-6454. URL https://www.sciencedirect.com/science/article/pii/S1359645420306509.

[49] M. M. Nygård, Ø. S. Fjellvåg, M. H. Sørby, K. Sakaki, K. Ikeda, J. Armstrong, P. Vajeeston, W. A. Sławiński, H. Kim, A. Machida, Y. Nakamura, and B. C. Hauback. The average and local structure of TiVCrNbDx (x=0,2.2,8) from total scattering and neutron spectroscopy. Acta Materialia, 205:116496, Feb 2021. ISSN 1359-6454. URL https://www.sciencedirect.com/science/article/pii/S1359645420309216.

[50] M. M. Nygård, G. Ek, D. Karlsson, M. Sahlberg, M. H. Sørby, and B. C. Hauback. Hydrogen storage in high-entropy alloys with varying degree of local lattice strain. International Journal of Hydrogen Energy, 44(55):29140–29149, Nov 2019. ISSN 0360-3199. URL https://www.sciencedirect.com/science/article/pii/S0360319919312820.

[51] M. M. Nygård, G. Ek, D. Karlsson, M. H. Sørby, M. Sahlberg, and B. C. Hauback. Counting electrons - A new approach to tailor the hydrogen sorption properties of high-entropy alloys. Acta Materialia, 175:121–129, Aug 2019. ISSN 1359-6454. URL https://www.sciencedirect.com/science/article/pii/S1359645419303611.

[52] L. R. Owen and N. G. Jones. Lattice distortions in high-entropy alloys. Journal of Materials Research, 33(19):2954–2969, 2018. ISSN 0884-2914. doi: 10.1557/jmr.2018.322. URL https://www.cambridge.org/core/article/lattice-distortions-in-highentropy-alloys/A6725CBFB8104932F20B7BFC87512B74.

[53] V. Pacheco, G. Lindwall, D. Karlsson, J. Cedervall, S. Fritze, G. Ek, P. Berastegui, M. Sahlberg, and U. Jansson. Thermal Stability of the HfNbTiVZr High-Entropy Alloy. Inorganic Chemistry, 58(1):811–820, Jan 2019. ISSN 0020-1669. doi: 10.1021/acs.inorgchem.8b02957. URL https://doi.org/10.1021/acs.inorgchem.8b02957.

[54] K. B. Park, J.-Y. Park, Y. D. Kim, J.-I. Choi, H.-T. Im, J.-W. Kang, H.-S. Kang, T.-W. Na, and H.-K. Park. Study on hydrogen absorption and surface properties of TiZrVNbCr high entropy alloy. Intermetallics, 130:107074, Mar 2021. ISSN 0966-9795. URL https://www.sciencedirect.com/science/article/pii/S096697952030978X.

[55] K. A. Persson, B. Waldwick, P. Lazic, and G. Ceder. Prediction of solid-aqueous equilibria: Scheme to combine first-principles calculations of solids with experimental aqueous states. Phys. Rev. B, 85:235438, 06 2012. doi: 10.1103/PhysRevB.85.235438. URL /papers/physrevb2012-solidaqueous.pdf.

[56] E. J. Pickering and N. G. Jones. High-entropy alloys: a critical assessment of their founding principles and future prospects. International Materials Reviews, 61(3):183–202, Apr 2016. ISSN 0950-6608. doi: 10.1080/09506608.2016.1180020. URL https://doi.org/10.1080/09506608.2016.1180020.

[57] E. Protopopoff and P. Marcus. Surface Effects on Hydrogen Entry into Metals, book section 2, pages 105–148. CRC Press, third edition, 2012. ISBN 978-1-4200-9462-6. URL https://doi.org/10.1201/b11020.

[58] D. Pukazhselvan, V. Kumar, and S. K. Singh. High capacity hydrogen storage: Basic aspects, new developments and milestones. Nano Energy, 1(4):566–589, Jul 2012. ISSN 2211-2855. URL https://www.sciencedirect.com/science/article/pii/S2211285512001115.

[59] N. A. A. Rusman and M. Dahari. A review on the current progress of metal hydrides material for solid-state hydrogen storage applications. International Journal of Hydrogen Energy, 41(28):12108–12126, Jul 2016. ISSN 0360-3199. URL https://www.sciencedirect.com/science/article/pii/S0360319915311010.

[60] M. Sahlberg, D. Karlsson, C. Zlotea, and U. Jansson. Superior hydrogen storage in high entropy alloys. Scientific Reports, 6(1):36770, Nov 2016. ISSN 2045-2322. doi: 10.1038/srep36770. URL https://doi.org/10.1038/srep36770.

[61] B. Sakintuna, F. Lamari-Darkrim, and M. Hirscher. Metal hydride materials for solid hydrogen storage: A review. International Journal of Hydrogen Energy, 32(9):1121–1140, Jun 2007. ISSN 0360-3199. URL https://www.sciencedirect.com/science/article/pii/S0360319906005866.

[62] G. Sandrock. State-of-the-Art Review of Hydrogen Storage in Reversible Metal Hydrides for Military Fuel Cell Applications. 1997. URL https://apps.dtic.mil/sti/citations/ADA328073.

[63] G. Sandrock. A panoramic overview of hydrogen storage alloys from a gas reaction point of view. Journal of Alloys and Compounds, 293-295:877–888, Dec 1999. ISSN 0925-8388. URL https://www.sciencedirect.com/science/article/pii/S0925838899003849.

[64] B. Sarac, V. Zadorozhnyy, E. Berdonosova, Y. P. Ivanov, S. Klyamkin, S. Gumrukcu, A. S. Sarac, A. Korol, D. Semenov, M. Zadorozhnyy, A. Sharma, A. L. Greer, and J. Eckert. Hydrogen storage performance of the multi-principal-component CoFeMnTiVZr alloy in electrochemical and gas–solid reactions. RSC Advances, 10(41):24613–24623, 2020. doi: 10.1039/D0RA04089D. URL https://doi.org/10.1039/D0RA04089D.

[65] H. Shen, J. Zhang, J. Hu, J. Zhang, Y. Mao, H. Xiao, X. Zhou, and X. Zu. A Novel TiZrHfMoNb High-Entropy Alloy for Solar Thermal Energy Storage, 2019. ISSN 2079-4991. URL https://doi.org/10.3390/nano9020248.

[66] H. Shen, J. Hu, P. Li, G. Huang, J. Zhang, J. Zhang, Y. Mao, H. Xiao, X. Zhou, X. Zu, X. Long, and S. Peng. Compositional dependence of hydrogenation performance of Ti-Zr-Hf-Mo-Nb high-entropy alloys for hydrogen/tritium storage. Journal of Materials Science & Technology, 55:116–125, Oct 2020. ISSN 1005-0302. URL https://www.sciencedirect.com/science/article/pii/S1005030220300426.

[67] B. H. Silva, C. Zlotea, Y. Champion, W. J. Botta, and G. Zepon. Design of TiVNb-(Cr, Ni or Co) multi-component alloys with the same valence electron concentration for hydrogen storage. Journal of Alloys and Compounds, 865:158767, Jun 2021. ISSN 0925-8388. URL https://www.sciencedirect.com/science/article/pii/S0925838821001742.

[68] S. Sleiman and J. Huot. Effect of particle size, pressure and temperature on the activation process of hydrogen absorption in TiVZrHfNb high entropy alloy. Journal of Alloys and Compounds, 861: 158615, Apr 2021. ISSN 0925-8388. URL https://www.sciencedirect.com/science/article/pii/S0925838821000220.

[69] W. Steurer. Single-phase high-entropy alloys – A critical update. Materials Characterization, 162: 110179, Apr 2020. ISSN 1044-5803. URL https://www.sciencedirect.com/science/article/pii/S1044580319329134.

[70] K.-Y. Tsai, M.-H. Tsai, and J.-W. Yeh. Sluggish diffusion in Co–Cr–Fe–Mn–Ni high-entropy alloys. Acta Materialia, 61(13):4887–4897, Aug 2013. ISSN 1359-6454. URL https://www.sciencedirect.com/science/article/pii/S1359645413003431.

[71] M. Vezvaie, J. J. Noël, Z. Tun, and D. W. Shoesmith. Hydrogen Absorption into Titanium under Cathodic Polarization: An In-Situ Neutron Reflectometry and EIS Study. Journal of The Electrochemical Society, 160(9):C414–C422, 2013. doi: 10.1149/2.020309jes. URL https://doi.org/10.1149/2.020309jes.

[72] D. G. Westlake. Site occupancies and stoichiometries in hydrides of intermetallic compounds: Geometric considerations. Journal of the Less Common Metals, 90(2):251–273, Apr 1983. ISSN 0022-5088. URL https://www.sciencedirect.com/science/article/pii/0022508883900759.

[73] X. Xin, R. Johansson, M. Wolff, and B. Hjörvarsson. Hydrogen in vanadium: Site occupancy and isotope effects. Phys. Rev. B, 93:134107, Apr 2016. doi: 10.1103/PhysRevB.93.134107. URL https://link.aps.org/doi/10.1103/PhysRevB.93.134107.

[74] J.-W. Yeh, S.-K. Chen, S.-J. Lin, J.-Y. Gan, T.-S. Chin, T.-T. Shun, C.-H. Tsau, and S.-Y. Chang. Nanostructured High-Entropy Alloys with Multiple Principal Elements: Novel Alloy Design Concepts and Outcomes. Advanced Engineering Materials, 6(5):299–303, May 2004. ISSN 1438-1656. doi: 10.1002/adem.200300567. URL https://doi.org/10.1002/adem.200300567.

[75] J.-W. Yeh. Overview of High-Entropy Alloys, pages 1–19. Springer International Publishing, Cham, 2016. ISBN 978-3-319-27013-5. doi: 10.1007/978-3-319-27013-5_1. URL https://doi.org/10.1007/978-3-319-27013-5_1.

[76] V. Zadorozhnyy, B. Sarac, E. Berdonosova, T. Karazehir, A. Lassnig, C. Gammer, M. Zadorozhnyy, S. Ketov, S. Klyamkin, and J. Eckert. Evaluation of hydrogen storage performance of ZrTiVNiCrFe in electrochemical and gas-solid reactions. International Journal of Hydrogen Energy, 45(8):5347–5355, Feb 2020. ISSN 0360-3199. URL https://www.sciencedirect.com/science/article/pii/S0360319919324577.

[77] C. Zhang, Y. Wu, L. You, X. Cao, Z. Lu, and X. Song. Investigation on the activation mechanism of hydrogen absorption in TiZrNbTa high entropy alloy. Journal of Alloys and Compounds, 781:613–620, Apr 2019. ISSN 0925-8388. URL https://www.sciencedirect.com/science/article/pii/S092583881834667X.

[78] C. Zhang, A. Song, Y. Yuan, Y. Wu, P. Zhang, Z. Lu, and X. Song. Study on the hydrogen storage properties of a TiZrNbTa high entropy alloy. International Journal of Hydrogen Energy, 45(8):5367–5374, Feb 2020. ISSN 0360-3199. URL https://www.sciencedirect.com/science/article/pii/S0360319919321299.

[79] J. Zhang, P. Li, G. Huang, W. Zhang, J. Hu, H. Xiao, J. Zheng, X. Zhou, X. Xiang, J. Yu, H. Shen, S. Li, and X. Zu. Superior Hydrogen Sorption Kinetics of Ti0.20Zr0.20Hf0.20Nb0.40 High-Entropy Alloy, 2021. ISSN 2075-4701. URL https://doi.org/10.3390/met11030470.

[80] Y. Zhang, Y. Zhou, J. Lin, G. Chen, and P. Liaw. Solid-Solution Phase Formation Rules for Multi-component Alloys. Advanced Engineering Materials, 10(6):534–538, 2008. doi: https://doi.org/10.1002/adem.200700240. URL https://onlinelibrary.wiley.com/doi/abs/10.1002/adem.200700240.

[81] X. W. Zhou, F. El Gabaly, V. Stavila, and M. D. Allendorf. Molecular Dynamics Simulations of Hydrogen Diffusion in Aluminum. The Journal of Physical Chemistry C, 120(14):7500–7509, Apr 2016. ISSN 1932-7447. doi: 10.1021/acs.jpcc.6b01802. URL https://doi.org/10.1021/acs.jpcc.6b01802.

[82] C. Zlotea, M. A. Sow, G. Ek, J.-P. Couzinié, L. Perrière, I. Guillot, J. Bourgon, K. T. Møller, T. R. Jensen, E. Akiba, and M. Sahlberg. Hydrogen sorption in TiZrNbHfTa high entropy alloy. Journal of Alloys and Compounds, 775:667–674, Feb 2019. ISSN 0925-8388. URL https://www.sciencedirect.com/science/article/pii/S0925838818337800.